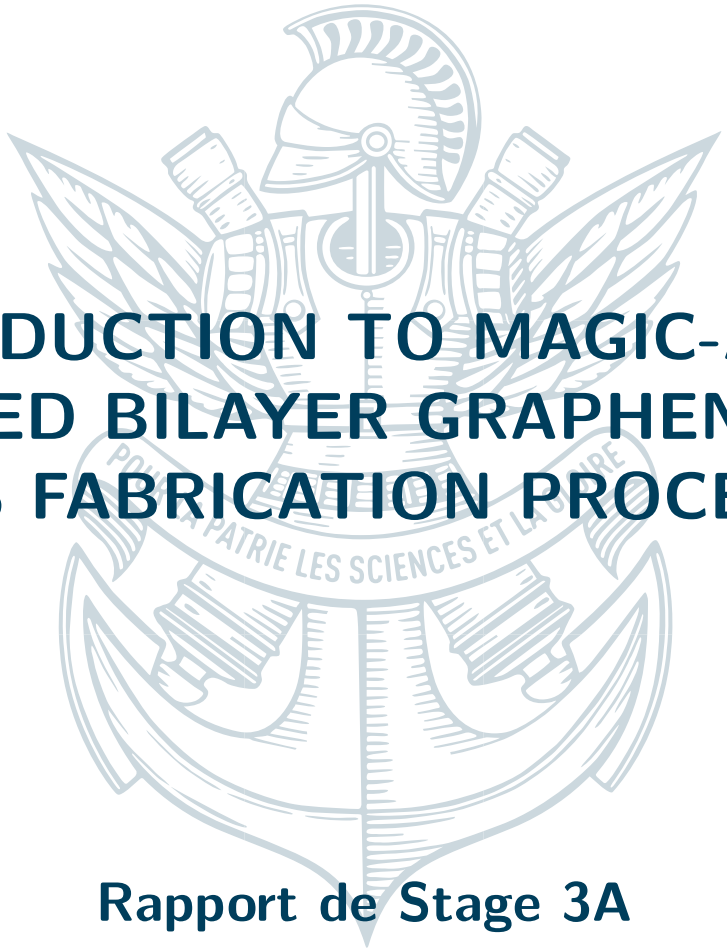

INTRODUCTION TO MAGIC-ANGLE TWISTED BILAYER GRAPHENE AND ITS FABRICATION PROCESS

Rapport de Stage 3A

Août 2023

Tuteurs : Prof. Dr. Dmitri K. Efetov, Dr. Alexandre Jaoui

Rémi Gilliot

ÉCOLE POLYTECHNIQUE

INSTITUT POLYTECHNIQUE DE PARIS

ABSTRACT

When stacking slightly twisted layers of graphene, we fabricate 2D materials, which exhibit tunable strongly correlated behaviors. As research is seeking for increasingly cleaner and more precise devices, we review the current complete fabrication process of magic-angle twisted bilayer graphene and we introduce several promising fabrication methods : flake identification, laser cutting, moiré imaging and anodic cutting. Amongst those, we report the implementation of graphene anodic oxidation, a groundbreaking new method allowing us to pattern 100 nm wide features. Our results represent a major improvement of the fabrication process of the group.

SUMMARY

Introduction **1**
Of 2D Materials and Twistronics . . . 1

1 Twisted Bilayer Graphene **3**
1.1 Moiré Patterns . . . 3
1.2 General Presentation . . . 4

2 Fabrication Process **12**
2.1 Exfoliation . . . 13
2.2 Flake Identification : Optical Microscope . . . 14
2.3 Stacking Previsualisation . . . 14
2.4 Cutting : Natural Stacking Cut and Manual Contact AFM Cutting . . . 16
2.5 Stacking Process . . . 18
2.6 Plasma Etching . . . 19
2.7 Evaporation of Metallic Contacts . . . 20
2.8 Chip Integration and Measurements Setup . . . 23

3 New Techniques Implementation **24**
Keeping on Improving the Fabrication Process of the Group . . . 24
3.1 Raman Flake Identification . . . 24
3.1.1 About the D Peak . . . 25
3.1.2 About the 2D Peak . . . 27
3.2 Raman for Laser Cutting . . . 29
3.3 AFM Moiré Imaging . . . 31
3.4 Anodic AFM Cutting . . . 31
Towards New Projects in the Group . . . 32

INTRODUCTION

Of 2D Materials and Twistronics

Since the discovery of graphene in 2004 [1], the study of 2D materials has proven to be very interesting and very fruitful. It paved the way for physicists to get privileged new insights on mechanisms at work in condensed matter.

First, the identification and the characterisation of graphene was already a revolution [2]. It truly was a disruptive revolution, because, from a physicist point of view, it showed that the materials properties can change drastically from 3D bulky crystals to 2D atomically thin systems. Also, from an engineer point of view, it opened many new possibilities by going beyond the idea that 2D materials were not thermodynamically stable.

Knowing this, researchers gained the opportunity to engineer custom-made van der Waals heterostructures, with combinations of various 2D materials stacked each one on top of the other, in order to create novel systems with interesting properties, both from a fundamental and applied standpoint. From all these new possibilities, several amazing subjects of research arose from the creation of original heterostructures. Here, we will present one of these custom-made heterostructures : magic-angle twisted bilayer graphene (MATBG), made out of several graphene and hexagonal boron nitride (hBN) layers.

First measured in 2018 [3], MATBG rapidly attracted a lot of attention, as it hosts a large panel of correlated phases of matter, combined with an excellent electronic tunability. This first great success led to research groups all around the world dedicating their fabrication focus to creating similar devices. Either by trying new designs of graphene heterostructures or by trying a similar design with other 2D materials, the main idea being that a 'twist' (rotating one or many layers of a certain angle) could completely transform the properties of the stacked layers. The field of research born of these investigations is nowadays usually called 'twistronics'.

In this report, we will discuss the reasons that have motivated researchers to take an interest in this particular novel device, dive into its full fabrication process and finally present the implementation of fabrication-related methods, that I've worked on. These two last chapters will be entirely focused on the methodology and research orientation of the Chair of 'Experimental Solid State Physics - Quantum Materials', a research group at the Ludwig-Maximilians-Universität in Munich, led by Prof. Dr. Dmitri K. Efetov.

1
TWISTED BILAYER GRAPHENE

1.1 Moiré Patterns

In this preliminary chapter, 2D moiré structures are introduced, in order to give a clearer subsequent overview of twisted bilayer graphene (TBG).

In custom-made heterostructures, moiré patterns is a core notion, at the heart of the considerations behind the devices properties. In 2D materials, a moiré pattern is a large-scale interference patterns, which naturally appears when stacked atomic layers are viewed from above. From this viewpoint, two examples are illustrated in figure 1. As highlighted, the large-scale interference pattern typically results from a slight crystallographic mismatch between the two stacked 2D lattices.

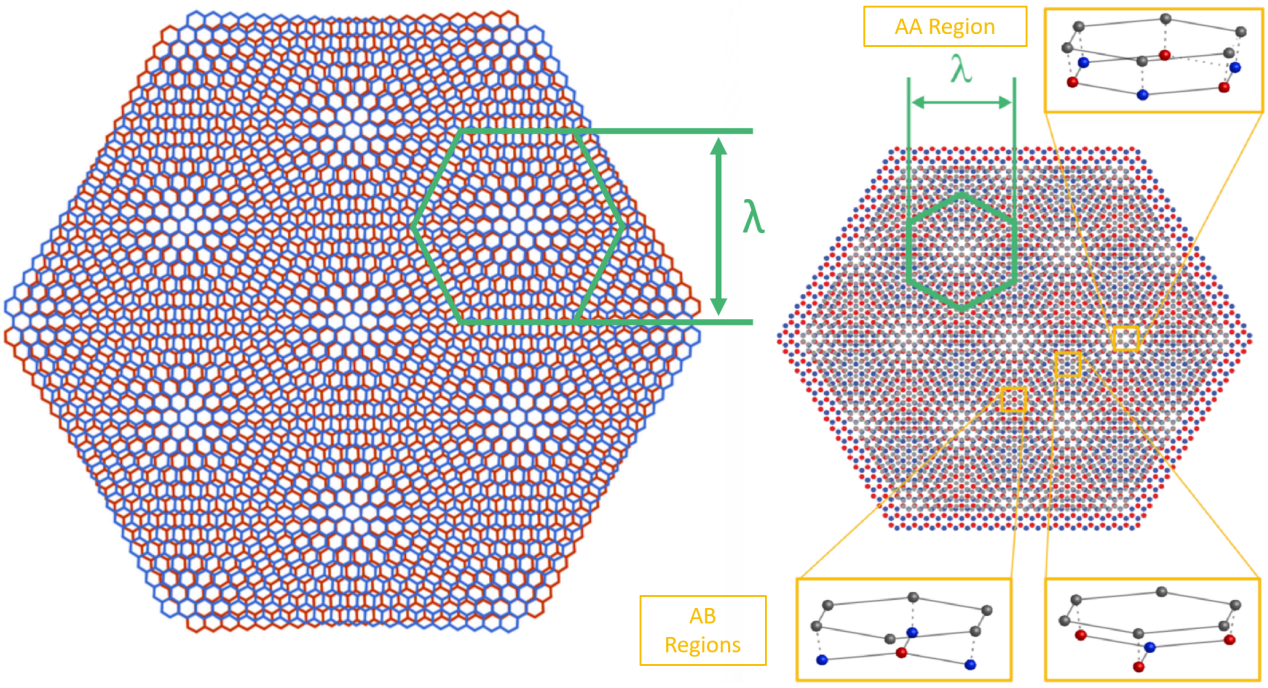

Figure 1: Schemes of two examples of moiré patterns : on the left is a typical moiré pattern appearing when two identical hexagonal layers are superimposed with a certain small angular mismatch and on the right is the one obtained when two aligned hexagonal layers with two slightly different lattice parameters are superimposed. The yellow insets show particular local crystallographic patterns [4]

.

From a more pragmatic perspective, the moiré pattern gives rise to an effective periodic super-potential, creating a new artificial 2D lattice. This new lattice corresponds to the overall periodicity of the stacked layers and is called a superlattice. The smaller the mismatch, the larger the superlattice unit cell and, accordingly, the smaller the corresponding Brillouin zone. As a result, owing to the dependence of the band structure on the Brillouin zone size, the material properties can deeply change as a function of the mismatch.

In our case, we will only consider heterostructures made out of graphene and hBN layers. As both lattices have the same hexagonal structure, the only possible sources of mismatch are the difference of lattice constants between hBN and graphene and the angular difference between the crystallographic axis of stacked layers. So, given this condition, however you combine these layers, the crystal structure cannot be altered and the overall superlattice will also be hexagonal, but it will have a different lattice constant, a_{super}.

These two possibilities are separately displayed in figure 1, where the superlattice unit cells are highlighted in green. First, on the left, an angular mismatch between two identical hexagonal layers is illustrated : it corresponds to the TBG case. If we consider, for instance, MATBG, having a twisting angle of 1.05°, an hexagonal superlattice emerges, with a lattice constant $a_{super} \approx 7.7$ nm and a unit cell size $\lambda_{super} \approx 13.4$ nm, i.e. 55 times the size of the graphene unit cell.

Secondly, on the right, a lattice constant mismatch between two non-twisted hexagonal layers is illustrated : it corresponds to the aligned graphene on hBN case. For instance, if we consider their lattice constants, respectively 0.142 and 0.145 nm, an hexagonal superlattice emerges, with a lattice constant $a_{super} \approx 6.9$ nm and a unit cell size $\lambda_{super} \approx 11.9$ nm, i.e. 48 times the size of the graphene unit cell.

1.2 General Presentation

The discovery of graphene already was amazingly interesting theoretically, its particular features being its two-dimensional nature coupled to its unique band structure. It was then deeply studied to overview the range of physical phenomena related with these features and, in particular, related to the Dirac points of its band structure (see figure 2).

Among all the unusual properties of graphene, we will mainly keep our focus on its electronic ones. Graphene shows metallic behavior with a significantly low charge carrier density, 10^{12} cm^{-2}, coupled to a very high carrier mobility, up to 100.000 $cm^2\ V^{-1}\ s^{-1}$, so that, under the right conditions, it exhibits ballistic conduction. Moreover, because of the Dirac points presence at its undoped Fermi level, graphene is called a zero-gap semiconductor and exhibits a tunable ambipolar conductivity [5] (see figure 3).

The linear dispersion of the Dirac cones also leads to electrons behaving as massless quasi-particles, accurately described by a 2D Dirac equation, in which the speed of light, c, is replaced by the Fermi velocity, v_F. This feature makes graphene a perfect platform, upon which to test quantum electrodynamics (QED) theoretical predictions, such as, for example, Klein Tunneling. Additionally, when immersed in a magnetic field, quantum Hall effect (QHE), fractional QHE and Hofstadter's butterfly have been observed for graphene [6].

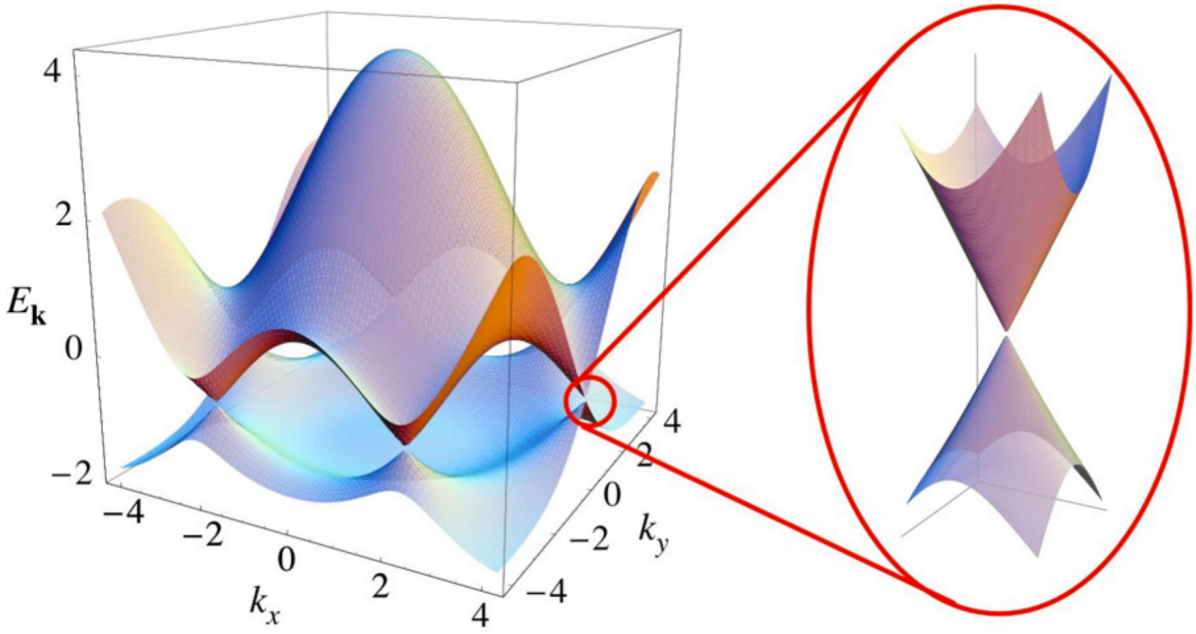

Figure 2: Band structure near the Fermi level of undoped graphene. The inset is a zoomed-in view of one of the Dirac cones [7].

But, besides QHE, it was still unclear why graphene doesn't exhibit any correlated behavior, despite its wide range of tunability and all its significant transport properties. Its unique band structure and density of states (DOS) were predicted and hoped to hold correlated phases of matter [8]. According to the main idea that sharpness or flatness of the Fermi surface tends to enhanced correlated phenomena [9], physicists were trying to capitalise on the Van Hove singularities of graphene DOS. And, among every possible correlated phases, they were particularly trying to induce superconductivity [10].

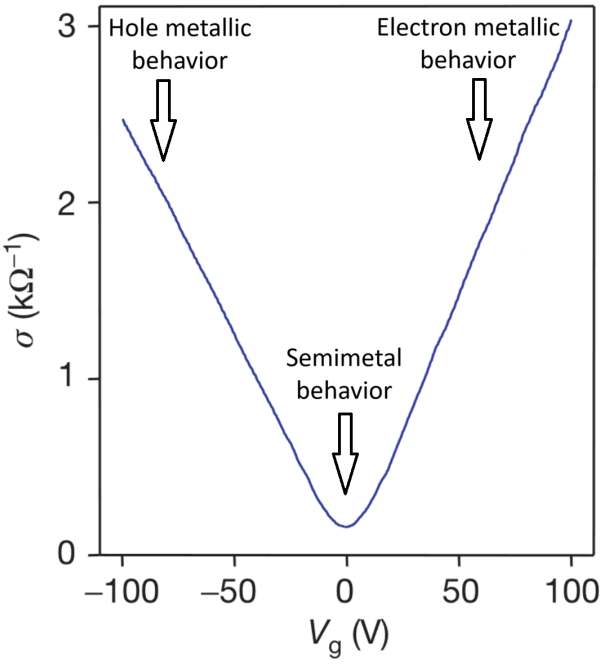

Figure 3: Graph representing the electric field effect in graphene. Here, one can see the dependence of the conductivity of graphene, σ, on the applied gate voltage, V_g [2].

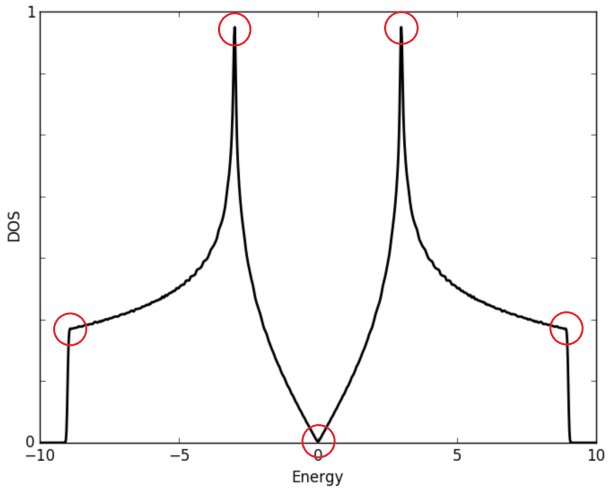

Figure 4: Normalised DOS of Graphene as a function of energy (in eV). The Fermi level is taken as the zero energy level. In red are highlighted the visible Van Hove singularities of graphene [11].

However, even until now, no such behavior has been observed for pure graphene, a significant obstacle being the vast energy gaps isolating each Van Hove singularities, too large to be attained by gating the graphene layer (see figure 4). So, in order to achieve inducing superconductivity in a graphene-based device, research groups chose to explore many different ideas, one of which was to fabricate moiré patterned devices. This idea consisted of making use of the already well-known moiré theory for optics and to apply it to condensed matter physics. It would let one be able to tune even more the electronic properties of its device, by tuning the overall moiré superlattice unit cell (its size and its arrangement). For graphene-based devices, it naturally took the form the form of a twist during the fabrication process.

This plan has rapidly been supported by principle measurements of naturally twisted graphene layers, which appear, for example, in graphene grown by chemical vapour deposition (CVD). These local measurements were made trough scanning tunelling microscopy (STM) and revealed two important points : first, TBG was stable at standard temperature and pressure, even at twisting angles as low as 1.16° and, secondly, the device band structure does actually depend on the twisting angle and the induced modifications are profound enough to reduce the gaps in between Van Hove singularities to tens of millielectron-volts [12].

At the same time, theoretical description of TBG band structure was already well underway. The first calculations were going in the same direction as these measurements, by predicting that Fermi level bands of TBG were becoming very flat for very small twisting angles. Furthermore, their structure was keeping the main features of graphene DOS : the Dirac cone feature, whose Fermi velocity was much smaller, leading to much lower energy dispersion, and several Van Hove singularities [13][14]. So, eventually, the flatness of these bands became a more suitable approach to describe in a few words how close Van Hove singularities were from one another, but also from the Fermi level.

Finally, in 2011, these various theoretical works led to an amazing result : an accurate calculation of the dependence of the Fermi velocity on the twisting angle. It showed a series of discrete minimum at certain twisting angles, for which the bands were the flattest and the DOS, the densest (see figures 5 and 6). Therefore, large electron-electron interactions were predicted to arise and correlated phases of matter, to emerge, at these particular, magic angles [15][14].

From that moment on, with these results, it seemed clear that TBG really was a very promising materials and that these flat bands, tens of millielectron-volts wide, could hosts strongly correlated states. But, in order to measure and to ascertain MATBG properties, fabrication processes had first to be refined.

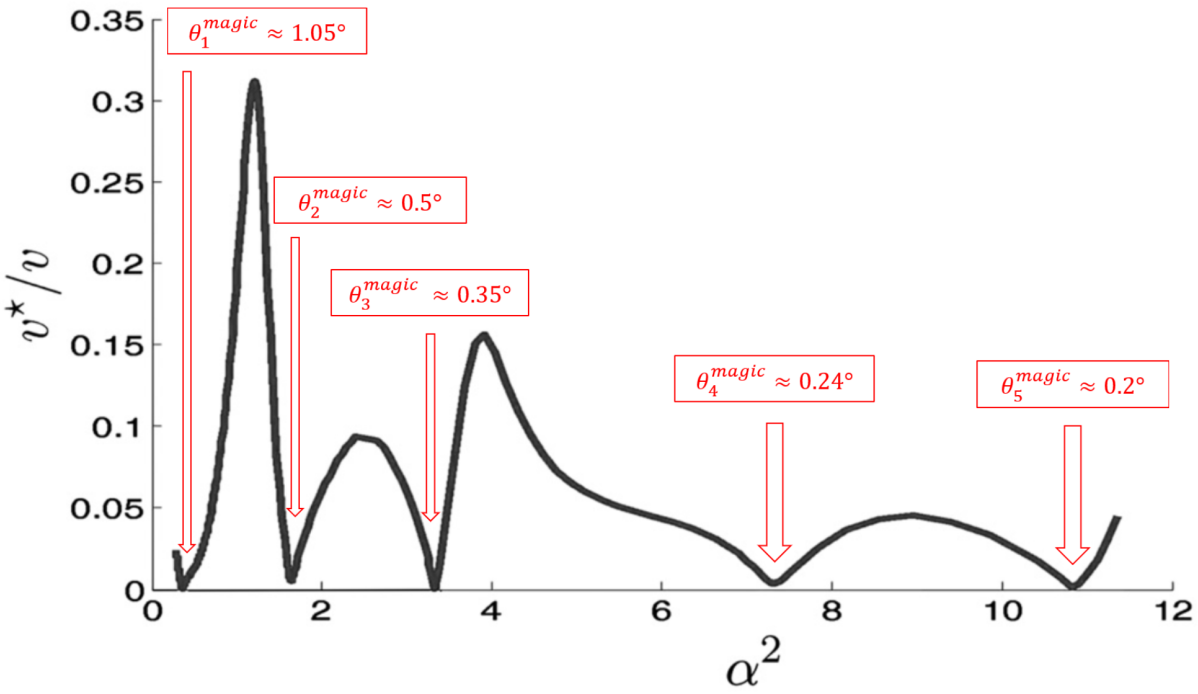

Figure 5: Graph representing the normalised Fermi velocity as a function of a dimensionless parameter, α, defined such that $\alpha^2 = (\frac{w}{\hbar v k_\theta})^2 \propto sin(\frac{\theta}{2})^{-2}$. This part of the curve shows only the first five minima [14].

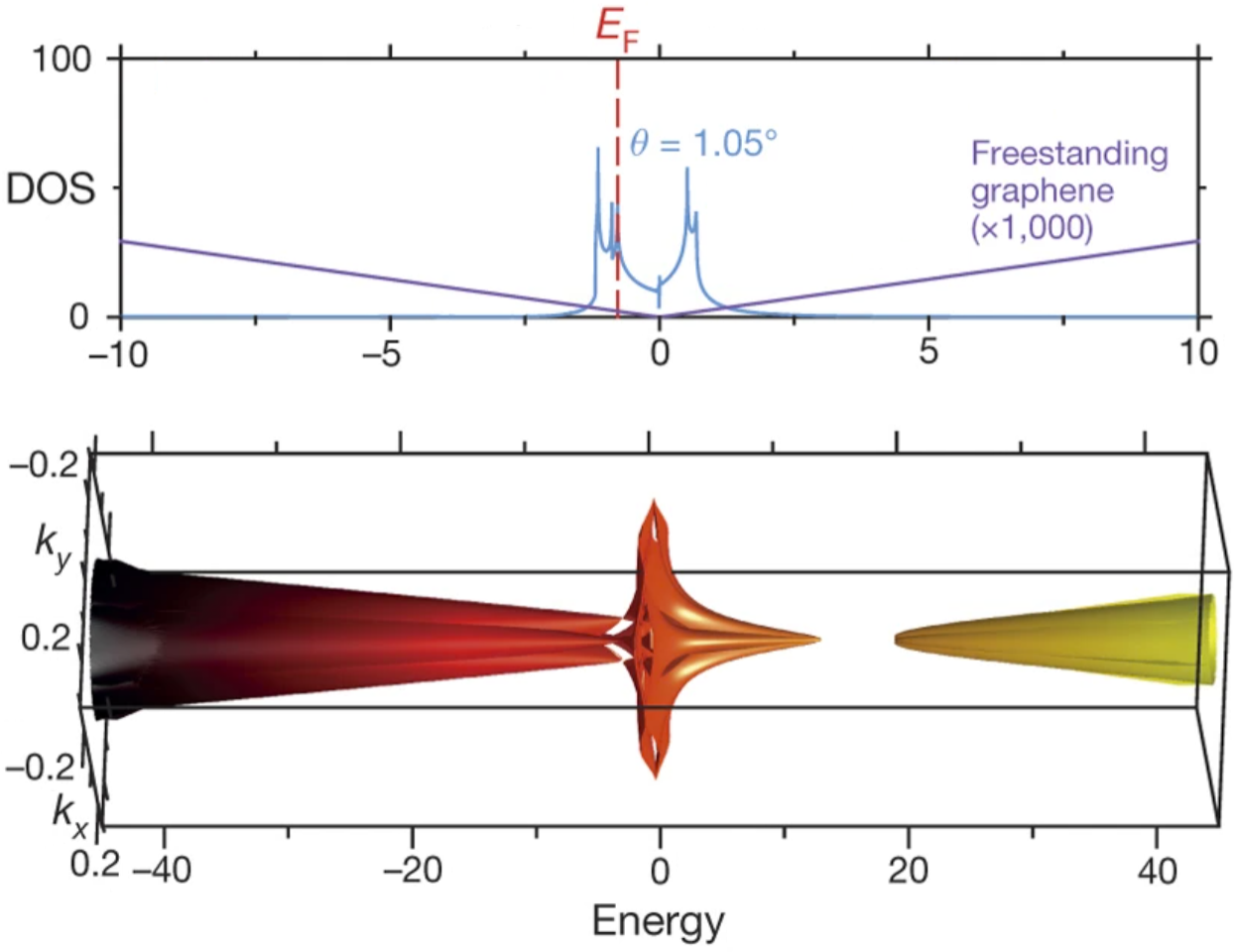

Figure 6: DOS and Band Structure (from top to bottom) of magic angle twisted bilayer graphene for the first magic angle of 1.05°. We can easily compare the MATBG DOS and the graphene DOS and see how the states are concentrated around the Fermi level. The energy is expressed in units of meV, the wave vectors, in nm^{-1} and the DOS, in eV^{-1} nm^{-2}. The Fermi level of graphene is taken as the zero energy level and the Fermi level of MATBG is highlighted in red [3].

First MATBG devices were finally achieved in 2018 and lived up to scientific expectations, by exhibiting exotic electronic states. Since then, the fabrication process was spread and incorporated into the expertise of several experimental groups, which also succeeded to create MATBG devices. The initial measurements were subsequently reproduced, then exceedingly extended. And these exceptional results eventually led to induct MATBG into the hall of fame of condensed matter [3][16].

Today, the interest for MATBG is still growing : numerous research groups around the world now contribute to the fabrication and measurements of MATBG devices, yielding up to thousands of articles per couple of years.

Currently, research is dedicated mainly to the first magic angle, $\theta_1^{magic} \approx 1.05°$, and to a lesser extent to the second magic angle, $\theta_2^{magic} \approx 0.5°$. The reason is twofold ; first, the feasibility decreases a lot as the angle approaches zero, due to the angular inaccuracy and to relaxation phenomena. Secondly, the first magic angle is predicted to be the most interesting, by having the 'flattest' flat bands as well as well-defined outer bands, very far from the Fermi level.

The phase space of first magic angle TBG is therefore being thoroughly explored and it has already uncovered many relevant behaviors. Among them, one can find QHE, strange metal behavior, ferromagnetism, electronic nematicity, Chern insulator states, correlated insulator behavior and superconductivity (see figures 8, 9 and 7).

These behaviors aren't new by themselves, but, within a single MATBG device, the ease with which each one of them can be seen, just by tuning outer measurement parameters, makes it much simpler to study these different behaviors experimentally. What's more, from a theoretical point of view, their proximity challenges current models and calls into question our understanding of the underlying phenomena.

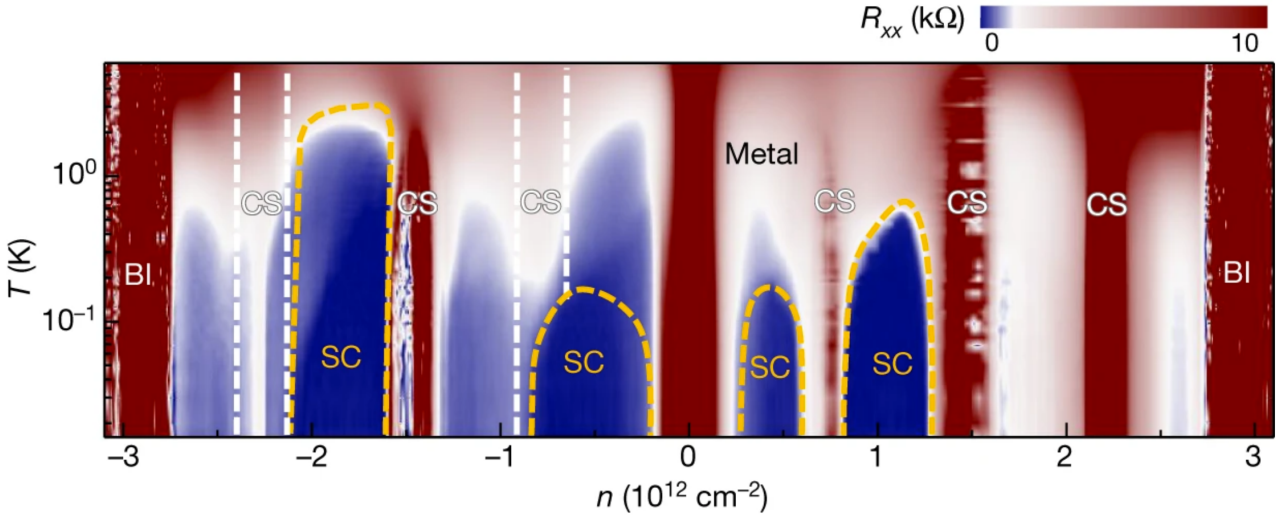

Figure 7: Phase space of MATBG longitudinal resistance, R_{xx}, as a function of temperature, T, and electronic density, n (tuned by changing the gate voltage). Here, one can see superconductive states (SC), correlated insulator states (CS) and band insulator state (BI) [17].

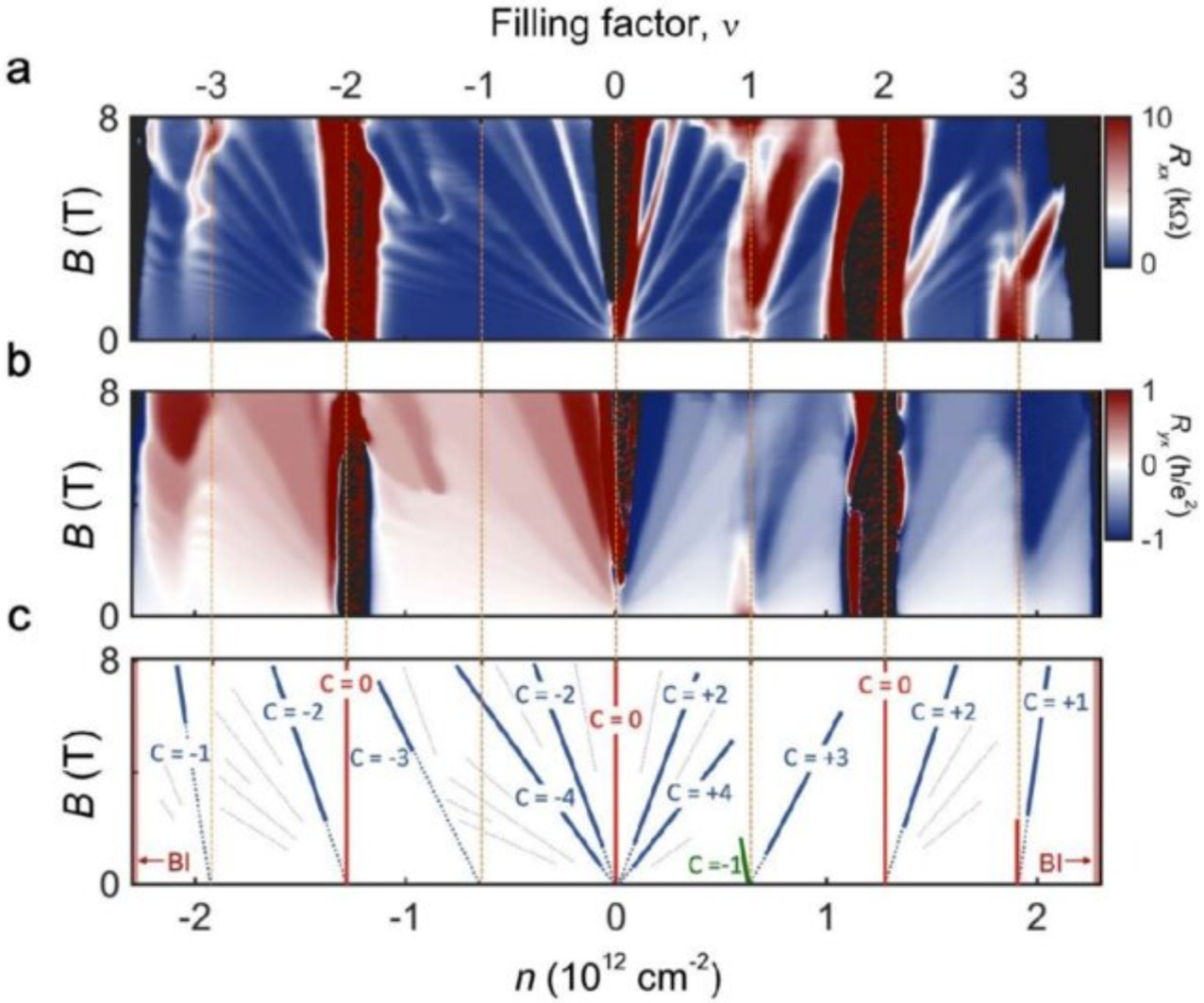

Figure 8: Example of MATBG Chern insulator states : (a) and (b) represents respectively the phase space of MATBG longitudinal and Hall resistances, R_{xx} and R_{xy}, as a function of magnetic field, B, and electronic density, n (tuned by changing the gate voltage). In (a), one can see the Chern insulator states, whose higher resistances form lines (in light red or white), disrupting MATBG conductive phases (in blue). (c) represents the associated phase diagram, in which solid lines correspond to specific well developed Chern insulator states : they exhibit a quantized Hall conductance $\sigma_{xy} = R_{xy}^{-1} \approx C * \frac{e^2}{h}$, where $\frac{e^2}{h}$ is the von Klitzing constant, also called the conductance quantum, and C is the state-characterising Chern number. Grey dashed lines show other quantum Hall states. The temperature is fixed at $T = 50$ mK [18].

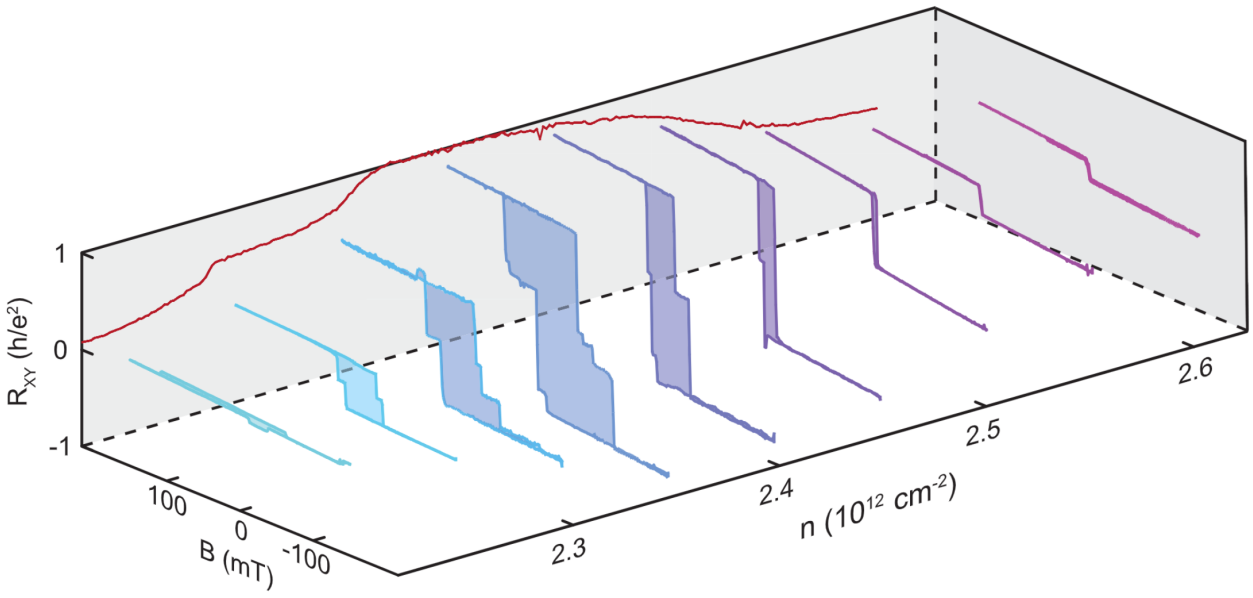

Figure 9: Example of MATBG ferromagnetism and anomalous QHE : the behavior of the Hall resistance, R_{xy}, as a function of magnetic field (along the z direction), B, and of electronic density, n (tuned by changing the gate voltage), is shown. At n fixed, B is swept one way, then the other, showing hysteresis behavior (hysteresis area is shaded). This ferromagnetic behavior is combined with a stable value of $R_{xy} \approx \frac{h}{e^2}$ at zero magnetic field, showing anomalous QHE with a quantized Hall conductance, $\sigma_{xy} = R_{xy}^{-1} \approx 1 * \frac{e^2}{h}$, where $\frac{e^2}{h}$ is the von Klitzing constant, also called the conductance quantum. The temperature is fixed at $T = 1.6$ K [19].

2
FABRICATION PROCESS

Fabrication is the first and, sometimes, the longest stage of an experimental project. As there are a lot of obstacles to overcome in order to get effective magic-angle devices, researchers are brought to develop an unique know-how through rinse and repeat kind of work.

The main concern to bear in mind throughout the whole fabrication process is about how clean and homogeneous is the device. The idea behind it is that the overall structure will naturally relax, giving a device with twist-angle inhomogeneity. So, if the sample is dirty, with defects, dirt particles or strain, for example, there won't be any continuous suitable channel going across the device. Without any mesoscale, clean and homogeneous channel, connecting (at least) two electrodes, no accurate transport measurement can be achieved.

The encapsulation of the device is preventing any decrease of its cleanliness, but only after the end of the stacking stage. So, to refine the device quality (cleanliness and homogeneity), technical improvements of the fabrication pre-stacking steps have always been looked for.

Up until now, research projects gradually went from studying MATBG to characterising numerous similar, but generally more complicated, graphene-based devices. These new devices are still characterised for their particular physical properties, but also with a focus on actual applications. We will be presenting here the complete fabrication process of one representative example : double-gated MATBG (see figures 10 and 11).

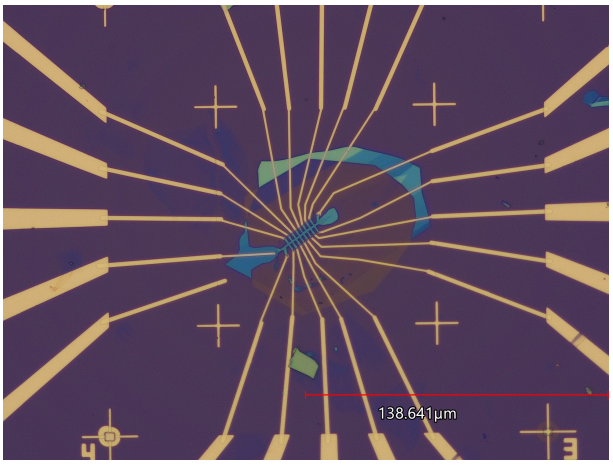

Figure 10: Microscope picture (x50) of the complete MATBG device.

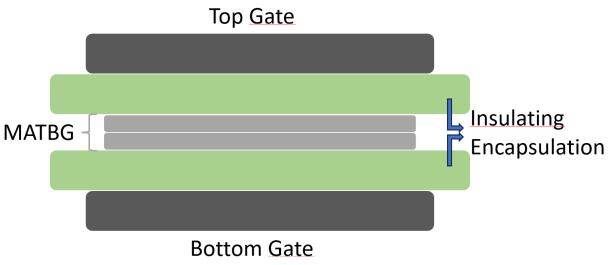

Figure 11: Sketch of double-gated MATBG : MATBG is encapsulated by insulating hBN and double-gated by few-layer graphene (FLG, crystal made of six to ten layers of graphene).

2.1 Exfoliation

The first step is to isolate the needed materials to form the van der Waals stack. As one can see on figure 11, we will need graphene for TBG, hBN to encapsulate it and few-layer graphene (FLG, crystal made of six to ten layers of graphene) for the gates.

In order to do that, mechanical exfoliation is the most appropriate method. It consists of repeated peeling of graphite, using scotch tapes, before transferring the exfoliated graphene layers from the tapes to silicon chips. The idea is to take advantage of the toughness difference between the weak vertical van der Waals bonds (interlayer bonds) and the strong horizontal covalent bonds (intralayer hexagonal bonds). So, the peeling of a graphite crystal leads to the crystal breaking along the vertical mechanically exceeded axis, in between two particular graphene layers, giving two crystals with a fewer number of layers.

Today, exfoliation is considered as the most appropriate method thanks to its unrivaled cleanliness : graphite is literally opened up in two, so immediately after exfoliating, graphene flakes are atomically clean. Moreover, the strength difference of intra and interlayer bonds is big enough to create very high quality graphene layers without any defect. This is why exfoliation is preferred to the other usual approach, chemical vapour deposition (CVD), which doesn't achieve such level of quality.

To optimise the process, prior to the exfoliation step, oxygen plasma is used to clean silicon chips of any adsorbed dirt particles. Thereby, by maximising the uniform contact area during the last peeling, when transferring exfoliated FLG from the scotch tape to the chip, one gets bigger flakes and a higher density of flakes [20] (see figure 12).

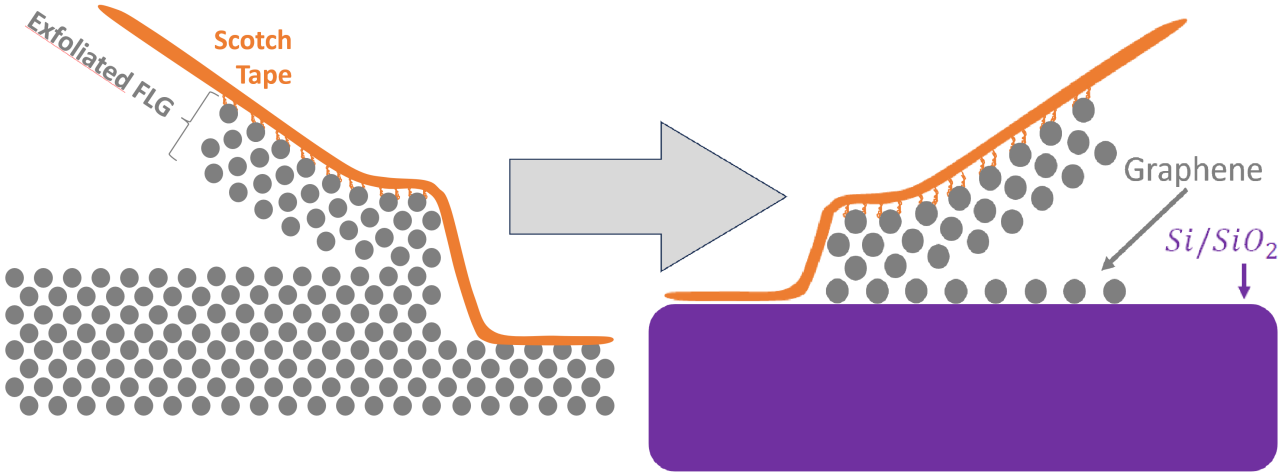

Figure 12: Scheme of two representative steps of mechanical exfoliation. On the left, scotch tape is used to exfoliate FLG from bulk graphite and, on the right, the same scotch tape is squeezed against a silicon chip (in purple), resulting in a layer of graphene being deposited.

2.2 Flake Identification : Optical Microscope

Optical microscopy is the most used method to identify exfoliated flakes, especially because of its readiness and its quickness. Only a classic microscope with a magnification of x20 is needed and seasoned PhD students only need few minutes to scan areas of tens of cm^2.

This easiness can be achieved thanks to the silicon chips. Optical studies showed that graphene layers were much more simpler to see on several particular substrates, one of them being a thermally oxidized silicon chip, made of a very thick Si layer, with a thin SiO_2 layer on top, usually around 285 nm for ideal graphene identification [21].

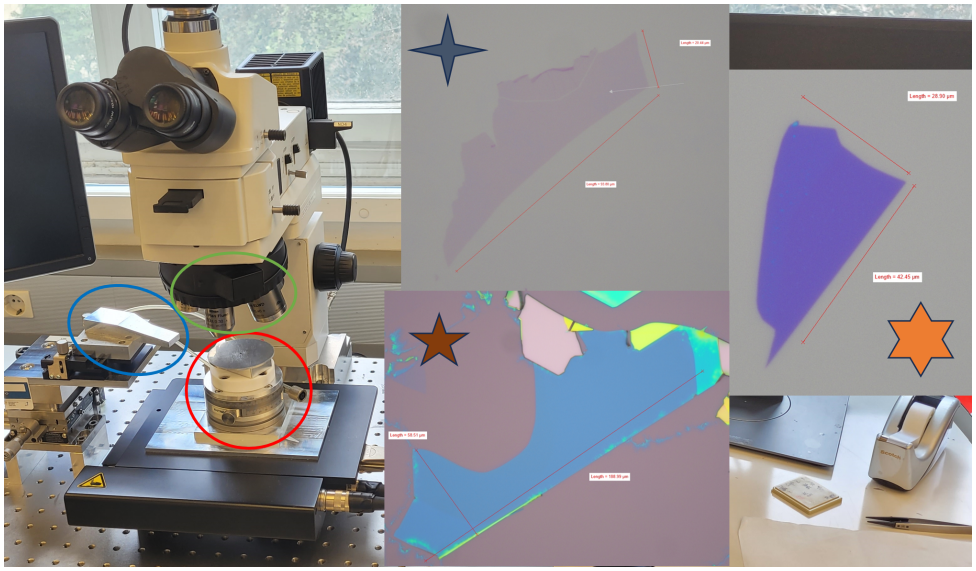

Figure 13: Picture of transfer stage equipped with an optical microscope. Green bordered are the microscope objectives, focused on the red bordered transfer stage. Blue bordered is the stamp holder, manually driven with precision micrometric screws. The insets show the optical identification of three example flakes. Dark cross picture corresponds to graphene, brown star one, to hBN and orange star one, to FLG.

2.3 Stacking Previsualisation

Now that all needed materials are ready, the flakes of each component (graphene, hBN and FLG) have to be sorted in order to determine which ones can be paired to form a proper stack.

Usually, the 'perfect' device, which is looked for, is approximately 20 by 10 micrometers. On one hand, this size matches very nicely with the envisioned Hall bar design, which is determined according to the last steps machine capabilities. It is also big enough for transport measurements to give accurate results about MATBG crystalline properties. On the other hand, bigger devices don't necessarily lead to better results, because of their increasing number of inhomogeneities, especially twist angle inhomogeneities.

First, for graphene, an excellent flake must be very clean, homogeneous in color and free from tape residues and defects. Ideally, it has clean, straight edges and it is isolated from any other thicker graphene flake. Additionally, as it will become twisted bilayer, it has to be twice as big as the projected device, so an excellent graphene flake is around 20 by 20 µm.

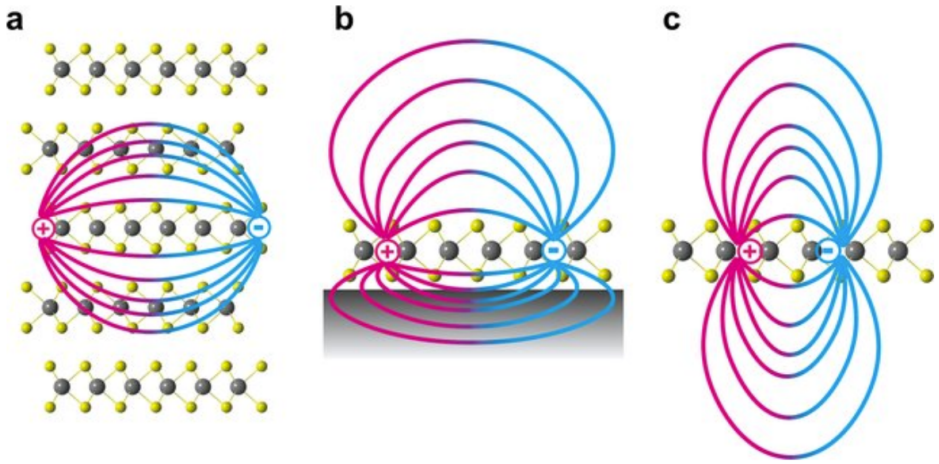

Figure 14: Sketch of example situations, showing the sensitivity to the environment of the Coulomb interaction between charged particles (represented here by electric field lines). In particular, this figure illustrates the case of MoS_2, another 2D material. (a) corresponds to multilayer MoS_2, (b), to monolayer MoS_2 on top of a dieletric material and (c) to freestanding monolayer MoS_2 [22].

Secondly, to encapsulate graphene, hBN is an excellent choice : it is a very good insulator and it has a crystalline structure identical to graphite, with hexagonal 2D lattices with strong covalent bonds and interlayer weak van der Waals bonds. Thus, hBN flakes are easy to exfoliate using the exact same method, they are also atomically clean after the exfoliation and they pair very well with graphene layers to create homogeneous van der Walls heterostructures. Moreover, it has be found in 2010 that hBN encapsulation led to much better transport properties in graphene based devices [23][24].

So, for hBN, an excellent flake is around 30 by 20 µm, bigger than the projected twisted bilayer to have a proper encapsulation. In particular, for a smooth stacking step, twisted bilayer shape has to fit in the hBN flake with a certain margin of maneuver. Ideally, its thickness must be enough to properly encapsulate and isolate MATBG from outer disturbances, but, at the same time, it must be relatively thin so as not to put too much pressure and strain on MATBG.

However, hBN thickness is a particularly delicate subject. In fact, it is noteworthy that the immediate environment of a 2D materials can influence its electronic properties, usually because of the screening of electric interactions (see figure 14). So, the hBN thickness, by determining the dieletric thickness and the distance to the metallic gates, has a direct influence on the device properties [25]. Nonetheless, even if it is interesting to highlight the impact of environment on the 3D Coulomb interaction in between MATBG 2D electrons, we can't really dive here into the question of the importance of this influence. While this subject is currently being studied, we will overlook these effects and consider that a good hBN thickness lies in between 10 to 30 nm.

Finally, for the gates, exfoliated FLG is an excellent choice : it is a byproduct of graphene exfoliation, it is also atomically clean, it has a metallic behavior and, as discussed before, it pairs very well with hBN. An excellent FLG flake is around 25 by 4 µm, longer and thinner than the projected twisted bilayer to simplify the metallic contacts evaporation step. Ideally, its thickness must again be as thin as possible for strain reason, but it also shouldn't influence MATBG transport measurements. To prevent this from happening, graphite gates can't be made of only one, two, three or four layers of graphene, which all have particular electronic behaviors. So, its perfect thickness lies in between 5 and 12 graphene layers, corresponding to a thickness of 1.5 to 4 nm.

2.4 Cutting : Natural Stacking Cut and Manual Contact AFM Cutting

Once every needed layer has been identified, the last preparation part is graphene cutting. The idea is that two distinct graphene flakes can't be used to fabricate TBG, because of their different unknown crystallographic orientations. That's why it is very important to cut a single flake into two parts with identical crystallographic axis, before twisting and stacking one above the other.

Originally, cutting was included during the stacking stage by using shearing forces naturally appearing between one half of the flake, attached to hBN, and the other half, attached to SiO_2 (see figure 15). But, this method led to many possible issues, decreasing the device quality. In particular, because of the strain induced at the edge of the flake, graphene can move while breaking, changing the relative angle between the two parts or even fold onto itself, preventing further proper stacking.

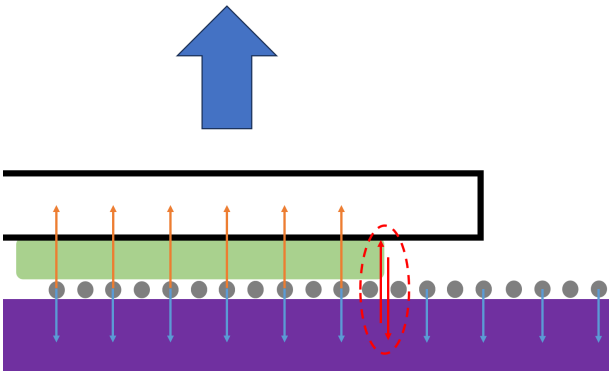

Figure 15: Sketch of uncut graphene lift-toff, when picked up by hBN. The stamp is black bordered and its motion follows the blue arrow. The hBN flake (in green) has already been picked up and has been laid down on one half of a graphene flake (in grey). Lifting forces, due to hBN-graphene van der Waals bonds (thin orange arrows), are competing with graphene-$Si0_2$ (in purple) van der Waals bonds (thin blue arrows), resulting in shearing forces (in red) building-up at the boundary.

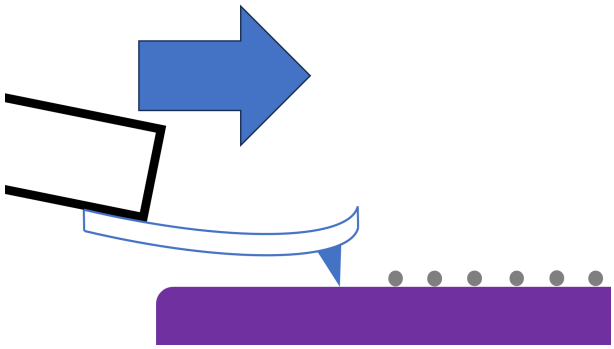

Figure 16: Sketch of manual AFM cutting. The stamp is black bordered and its motion follows the blue arrow. The AFM cantilever and tip are in blue; cantilever deflection results from a substantial contact force, sufficient to mechanically break graphene-$Si0_2$ (in grey and purple) van der Waals bonds. The AFM cutting sketch would be completely similar, the sole difference being that the stamp is replaced by a cantilever holder.

To achieve clean cuts, AFM cutting is currently the most widely used method. The idea is to use the AFM contact mode with a sufficiently high contact force, so that the AFM tip can cut graphene flakes when driven across them. This method induces much less strain and leads to cleaner flakes, but needs more time and resources.

However, to avoid using the AFM, this method can also be implemented manually : the tip is then fixed to a stamp (sticky substrate usually used to pick up the flakes) and moved manually using the transfer stage. To do this, the contact force can be estimated by looking at the deflection of the tip through the optical microscope and modified accordingly.

2.5 Stacking Process

As briefly discussed above, for the stacking step, a sticky substrate, called a stamp, is necessary. It is made up of a temperature-activated sticky layer, a polycarbonate (PC) film, above a soft cushion substrate, polydimethylsiloxane (PDMS). This centimeter-sized structure is attached to a large transparent glass plate, which is itself attached to the stamp holder (see figure 13).

The successive stacking steps are described in order in figure 17 and an example dropped stack is shown on figures 18 and 19.

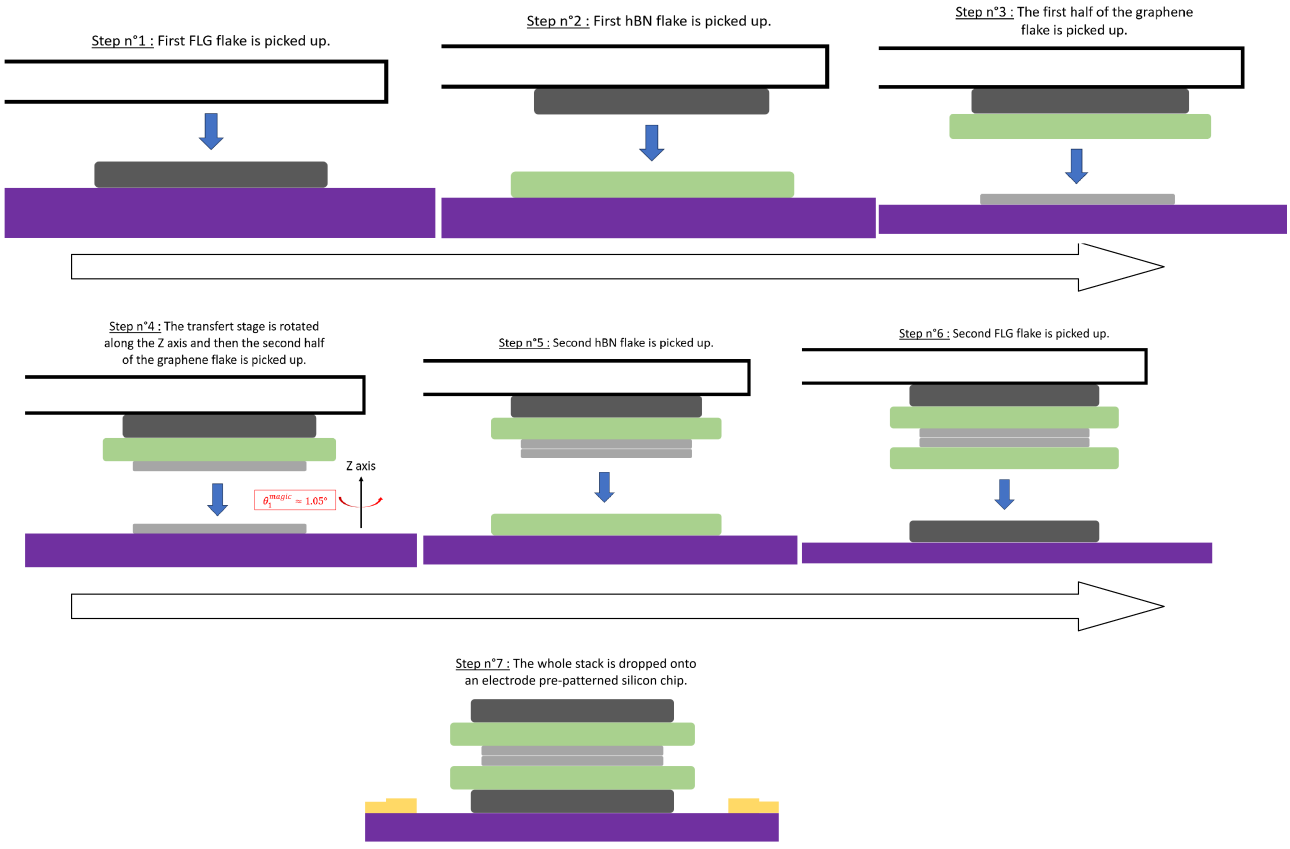

Figure 17: Usual stacking steps of fabrication process of a double-gated MATBG device. The last step, when dropping the full stack, is achieved by heating and melting the sticky polycarbonate (PC) film. So, the result illustrated at the seventh step corresponds to the state of the device after being chemically cleaned.

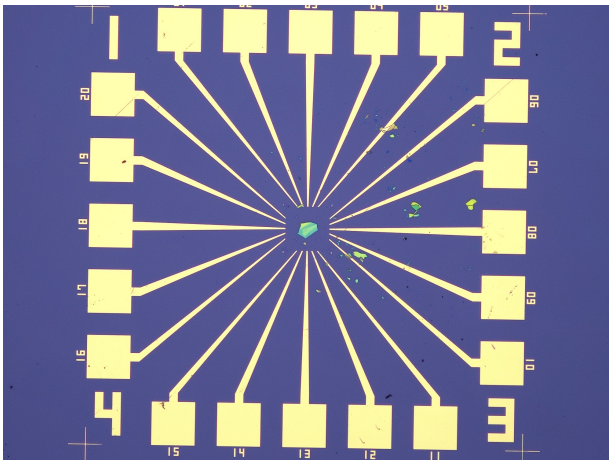

Figure 18: Optical microscope picture (x5) of a single-gated MATBG device at the end of the stacking stage. One can see the golden pre-patterned electrodes, which are going to be very useful to electrically contact the device.

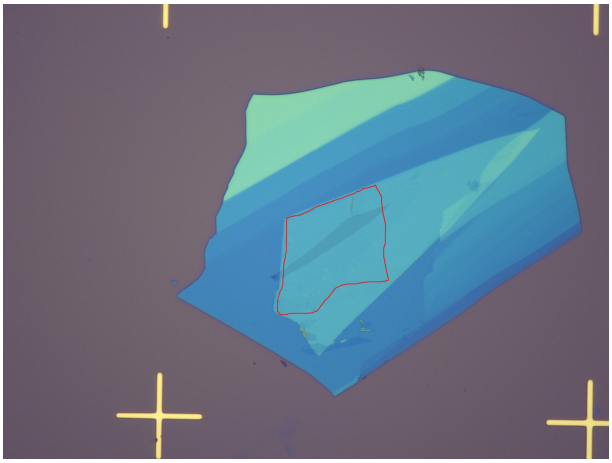

Figure 19: Optical microscope picture (x100) of a single-gated MATBG device at the end of the stacking stage. Both hBN flakes are clearly visible, while the thin graphite gate is not easy to see and the almost invisible graphene flakes have been red bordered.

2.6 Plasma Etching

At the end of the stacking process, what has been made is a big approximately rectangular chunk of stacked materials. Prior to the plasma etching step (also called reactive-ion etching), the final shape of the device has first to be determined, before the etching step carves the actual device out of this rectangle.

For transport measurements, devices are usually shaped like a Hall bar, composed of many legs (see figures 20 and 21). The legged shape matches very well with the four probes method, used for accurate resistivity measurements (either longitudinal or transverse resistivity), and an important leg density allows measurements to be made on several distinct channels, maximizing the probability to find relevant angle-homogeneous ones.

This particular shape is the reason why stacks are sought to have a long axis, which will become the 'body' of the Hall bar, while the other short axis will be regularly etched to become the 'legs'. An ideal Hall bar device would keep the full length of the graphene flakes, i.e. 20 µm, and would hold about ten legs on each side, with each leg width being between 1 and 2 µm.

Once the final layout of the device has been decided, the etching process can begin. First, the entire device is spin-coated with dissolved polymethyl methacrylate (PMMA), a polymer resistant to the plasma etching. Electron beam lithography (EBL) is then used to pattern the PMMA layer. As the EBL-exposed PMMA will be chemically removed with isopropanol (IPA), it has to be shaped like a reciprocal Hall bar, while the untouched PMMA, sticking on the device, forms the Hall bar mask.

When the Hall bar mask is ready, the CHF_3/O_2 plasma etching can take place. When the superfluous materials have all successfully been etched away, the chip is cleaned again using IPA and acetone. Finally, our MATBG device is now complete and only needs to be electrically connected, before measuring it.

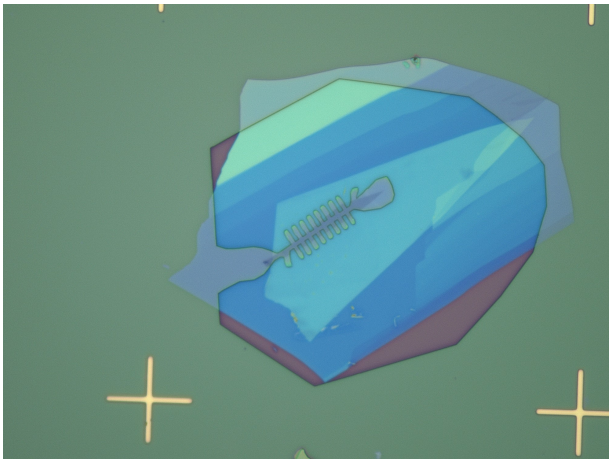

Figure 20: Optical microscope picture (x100) of the device right before the etching process. One can see the Hall bar PMMA mask left after the chemical cleaning.

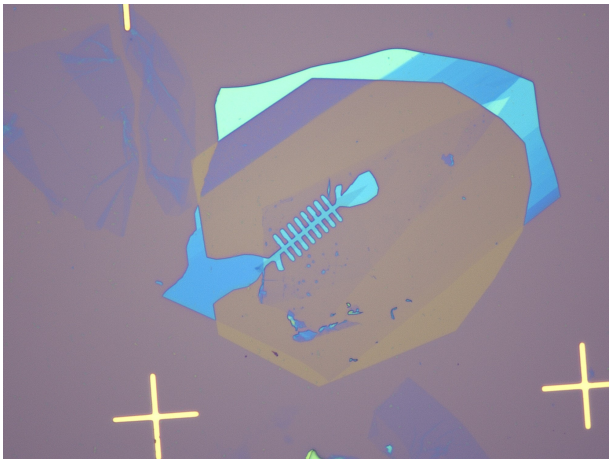

Figure 21: Optical microscope picture (x100) of the stack after the etching process and the chemical cleaning of the PMMA mask. One can recognise the Hall bar shape.

2.7 Evaporation of Metallic Contacts

As the device was dropped on a particular chip, with pre-patterned electrodes (see figures 18), the needed connections are only about 100 µm long. The straightforward evaporation method is then very well suited for this task.

The first step is to determine which material(s) will be used : it needs to be very conductive, to match well with graphene, so that the interface quality is very high and also not to exhibit any exotic electronic behavior at low temperatures. A very good combination of materials currently used by the group is gold on chromium, with a 5 nm thick evaporated layer of chromium and a 50 nm thick evaporated layer of gold above it [26].

Even if it is natural to think that hBN-encapsulated graphene layers cannot be easily reached, it has been shown that the CHF_3/O_2 plasma etching leads to tilted etched edges [27] (see figures 22 and 23). Then, now, the evaporation process can take place.

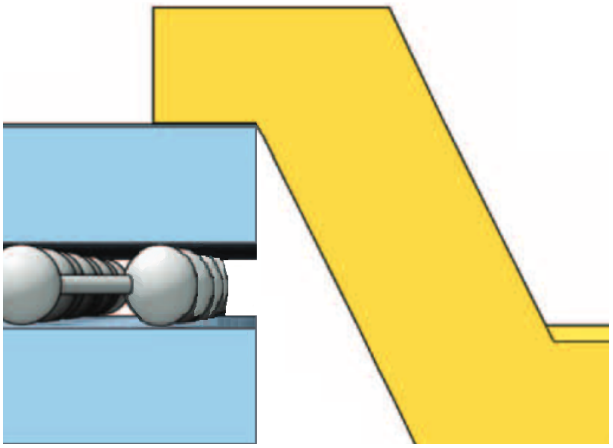

Figure 22: Sketch of etched device, using a etching process leading to straight edges. The evaporated metallic material (in yellow) is not touching the graphene and no electrical contact is made.

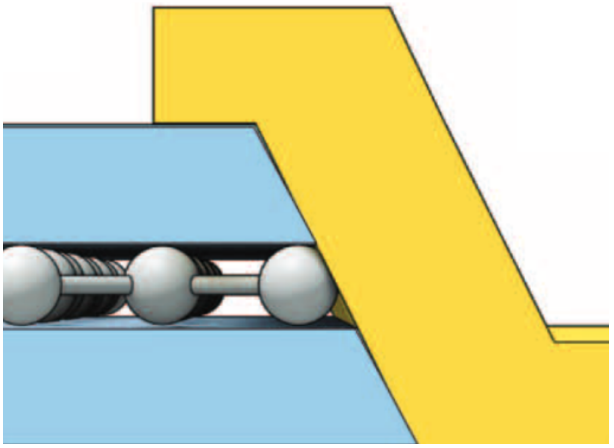

Figure 23: Sketch of etched device, using a etching process leading to tilted edges. The evaporated metallic material (in yellow) does touch the edge of the graphene flake, creating a 1D electrical contact.

The process is very similar to the previous etching one : the device is again spin-coated with PMMA, EBL is also used to pattern the PMMA layer and EBL exposed PMMA is then chemically removed. But, for evaporation, the removed part corresponds to where deposited materials will stick to the substrate, while the untouched PMMA will prevent deposited materials from touching the substrate. So, this time, the exposed part has to be shaped exactly as the wanted electrodes.

After the two-stages evaporation, superfluous deposited materials are cleaned away with the rest of the PMMA layer, using IPA and acetone. Our MATBG device is now connected to the chip electrodes and can now be manually measured (see figures 24 and 25).

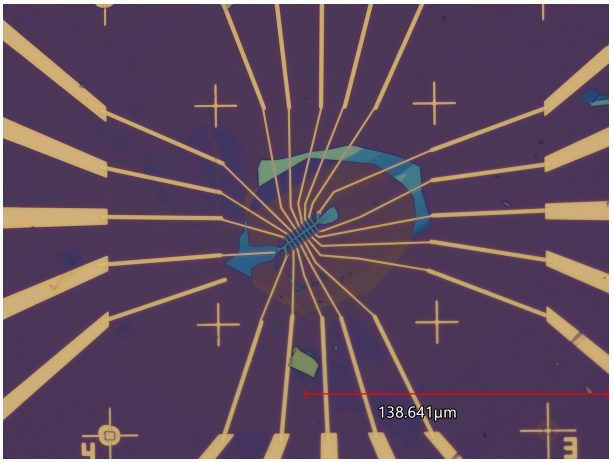

Figure 24: Optical microscope picture (x50) of the device after the evaporation process. One can see the freshly evaporated Cr/Au electrodes connecting the device to the pre-patterned electrodes.

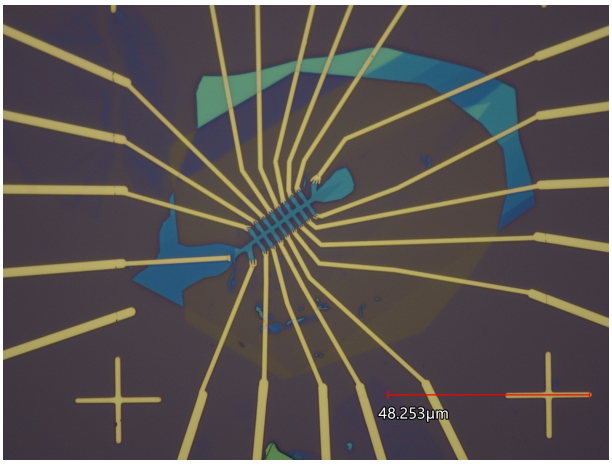

Figure 25: Optical microscope picture (x50) of the device after the evaporation process. One can see the freshly evaporated Cr/Au electrodes, paired to each and every legs of the device.

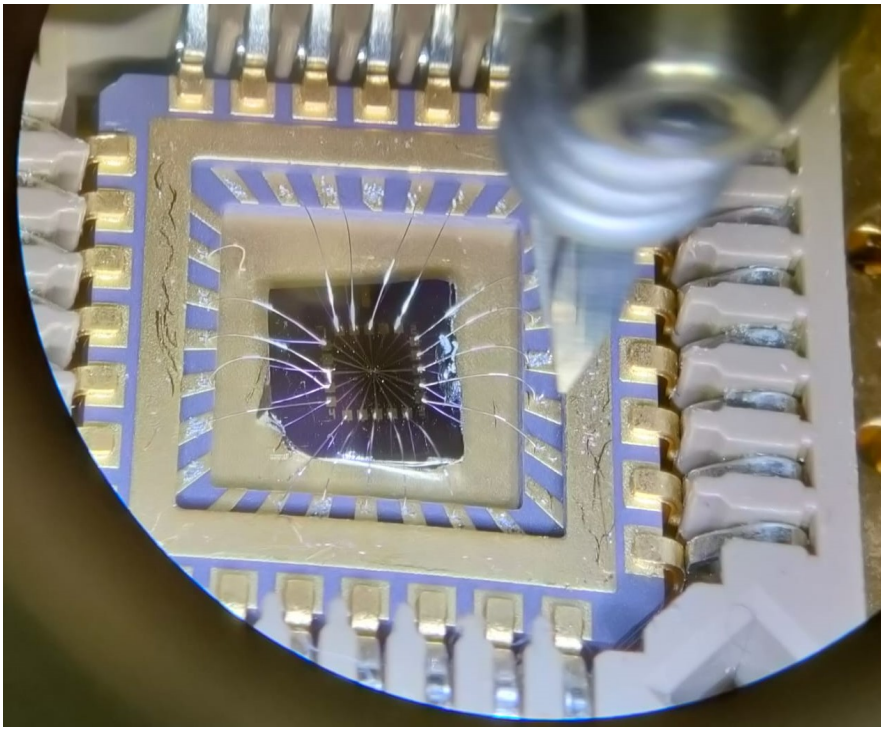

Figure 26: Picture of the final device, where one can see the dark purple electrode patterned initial chip, inside the light purple and golden chip holder. They are connected by the shining grey wire bonds surrounding the chip.

2.8 Chip Integration and Measurements Setup

However, in order to have it integrated within a general measurement setup, the electrodes patterned chip has to be put inside a setup-compatible chip holder. The chip holder has its own patterned electrodes, which matches with the setup electrodes.

Fortunately, this step doesn't require less than micrometer precision, as the electrodes being connected are macroscopic. But, as a trade-off, this task has to be carried out more manually, by using a wire bonding machine. Eventually, when the chip is integrated into the chip holder, MATBG device truly is complete and is ready to be measured (see figures 26 and 27).

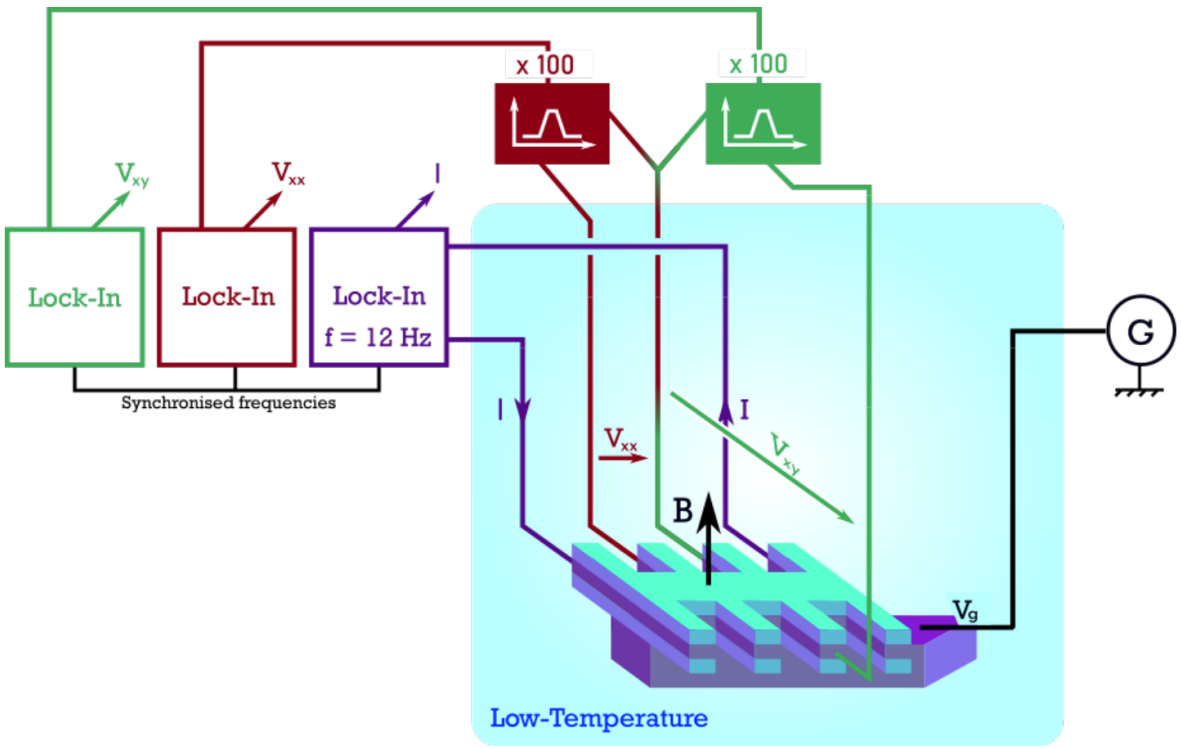

Figure 27: Sketch of the typical experimental setup. As illustrated, all the transport measurements are made using the lock-in method. Here, an example frequency, $f = 12$ Hz, is shown. One can see the 'master' lock-in (in purple), driving the voltage across the device, and the two measurements 'slave' lock-ins (in green and in red), measuring respectively the transverse and the longitudinal voltages. The low-temperature refrigerator (in light blue) is equipped with an electromagnet (usually superconducting), which allows out-of-plane magnetic field dependent measurements [28].

3
NEW TECHNIQUES IMPLEMENTATION

Keeping on Improving the Fabrication Process of the Group

This internship was an opportunity for me to work on new methods, which could prove useful for the fabrication of particular devices. Here, I will present Raman microscopy and atomic force microscopy (AFM), that I discovered through standard fabrication methods and worked on in order to implement new techniques.

3.1 Raman Flake Identification

Among the new systems, recently acquired by Efetov's group, the Raman microscope was the first system with which I became accustomed. The idea was first to explore the system capabilities and afterwards to determine their usefulness and the best way to incorporate them into the fabrication process. It was particularly important to discuss how these capabilities could allow the fabrication of new devices.

The Raman microscope is a system used for local microscopic Raman spectroscopy. It is made of an optical microscope, an excitation laser and a spectrometer. These are coupled in order to give access to the inelastic light scattering spectra emitted by a precisely chosen narrow region of the sample. The Raman microscope of the group is equipped with two lasers, a visible green laser (532 nm) and an infrared laser (1064 nm).

Graphene has already been extensively studied using Raman spectroscopy and numerous interesting effects has been uncovered. Here, we will discuss mainly about crystallographic information given by the D and 2D peaks of the Stokes graphene spectra (see figure 28).

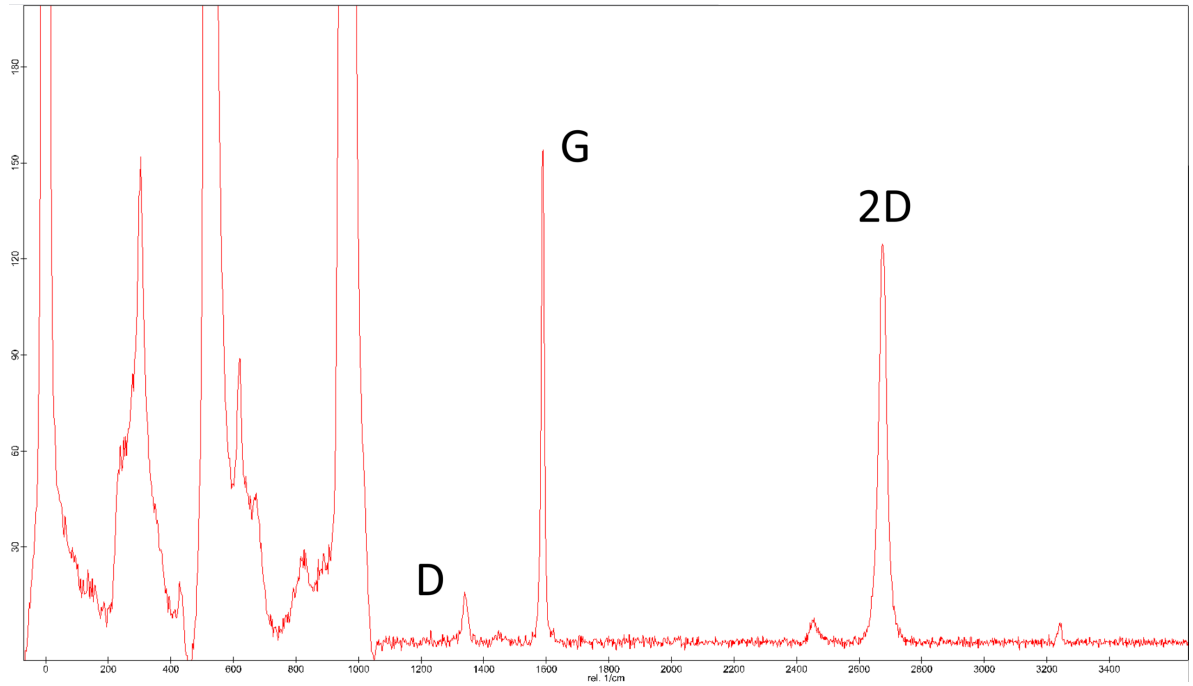

Figure 28: Measured Stokes graphene spectra : the first four thick peaks are Rayleigh scattering and Si/SiO_2 peaks and the three other most visible peaks are the D, G and 2D peaks of graphene.

3.1.1 • About the D Peak

The D peak is disorder-induced [29] : it doesn't appear in the spectra of homogeneous graphene regions, but only in disordered regions, presenting many defects. That makes it very useful, because crystallographic defects cannot always be detected using an optical microscope. Figures 29 and 30 illustrate cleanliness examination of a graphene flake using the D peak.

Moreover, the D peak can also appear at the edge of the flake and, for this type of anisotropic disorder, its intensity is dependent on the excitation laser polarisation. For graphene flakes, perfectly straight edges are either armchair or zigzag edges (see figure 31). It was predicted and measured that armchair edges gives a polarised-dependent D peak, while zigzag edges cannot contribute to the D peak [29]. This dependence is shown in figure 33.

As a result, the peak intensity shows maxima and minima, whose positions are related to the orientation of the edge. For the VV configuration, the maxima are found to happen when the polarisation of the incoming light and the armchair flake edge are parallel, offering very valuable insight on the flake structure. In fact, this method could be implemented in the group in order to determine precisely the crystallographic axis of a flake before the stacking step. The relevant point being that the different layer orientations in a device have an outstanding impact on the resulting moiré pattern and on the device properties. It would surely not be useful for graphene layers, which are already precisely twisted, but it would be very interesting in order to determine the hBN layers orientations.

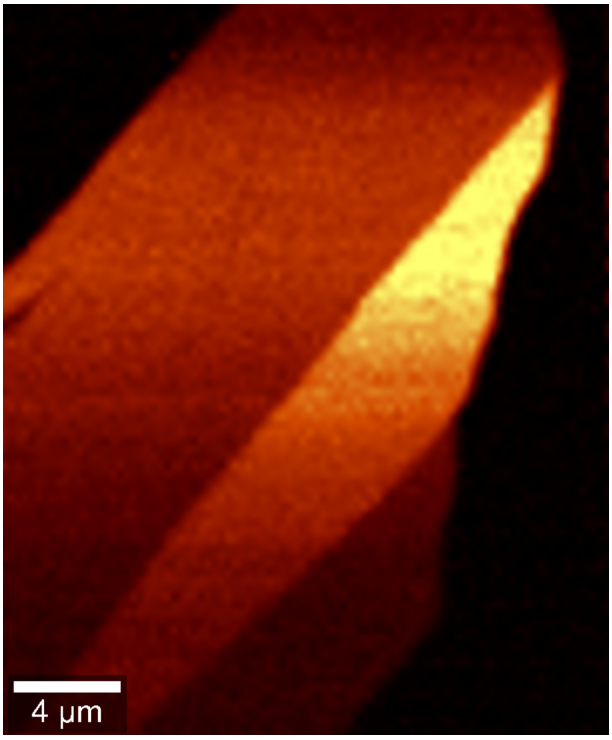

Figure 29: G peak intensity map of a graphene flake. One can see clearly the folding of the flake, but defects are almost invisible.

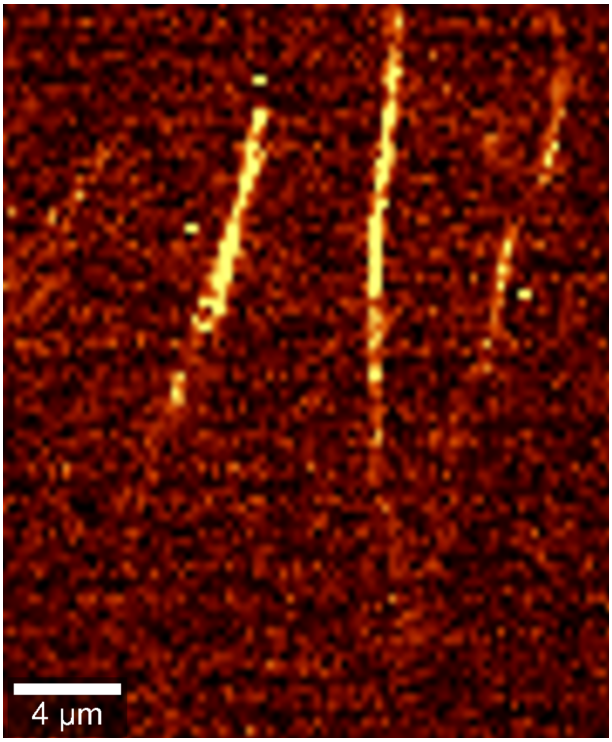

Figure 30: D peak intensity map of the exact same flake. One can now see clearly the defects of the flake.

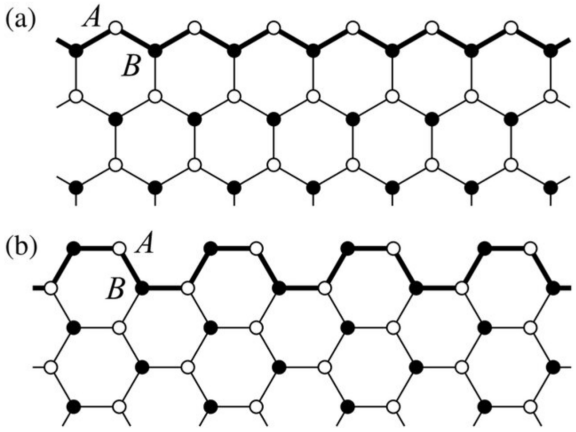

Figure 31: Zigzag and armchair edges of graphene (from top to bottom). One can hope to locally have one or the other only if the edge is straight. Usual imperfectly straight edges can be a wild combination of these two types [30].

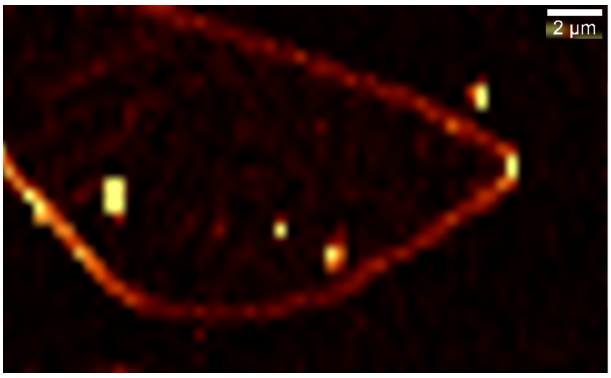

Figure 32: D peak intensity map of a graphene flake. One can see the edges of the flake, whose intensity relates to the edge armchair-likeness.

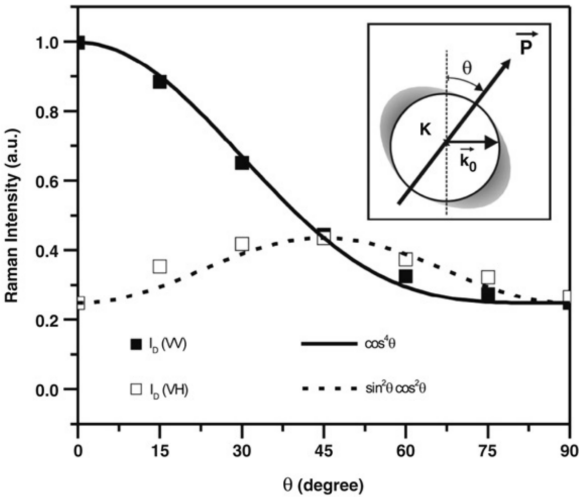

Figure 33: Normalised D peak intensity dependence as a function of the polarisation angle, θ. The situation $\theta = 0$ corresponds to a polarisation parallel to the studied edge. VV and VH respectively corresponds to aligned and orthogonal polariser-analyser configurations [31].

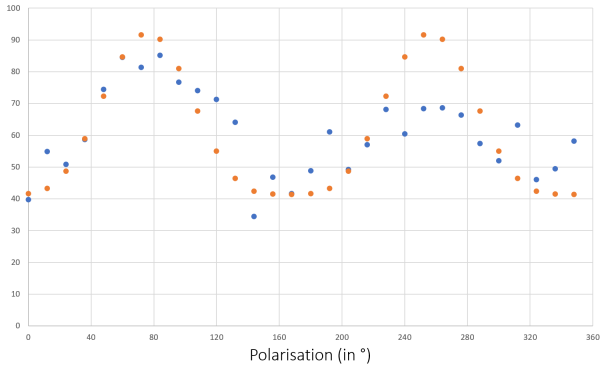

Figure 34: After finding an armchair edge with a significant D peak, we did a polarised dependence VV measurement (blue dots). According to the fitted data (orange dots), our graphene flake crystallographic axis are 16, 76 and 136° (to the horizontal axis of the Raman microscope).

3.1.2 • About the 2D Peak

The 2D peak, also sometimes called the G' peak, is well named, because it gives very valuable information about the local number of layers in a graphene flake and also about the stacking order of those layers.

First, for single layer graphene, the 2D peak appears as a thin Lorentzian, centered at 2687 cm^{-1}. On the contrary, thicker graphene flakes, from bilayer on, present much broader 2D peaks, fitted only by several Lorentzians around an average shifted center [29] (see figures 35 and 36).

However, this insight is limited to very few layers identification, as the 2D peak shapes of thicker flakes quickly become too similar to one another, in order to unquestionably differentiate them. Additionally, the group is already able to identify few layers graphene flakes optically, which is an easier method.

Nonetheless, from trilayer on, graphene flakes are found to naturally adopt one of two stable stacking orders : Bernal stacking (ABA) or rhombohedral stacking (ABC). This crystal structure difference has a significant impact on the shape of the 2D peak (see figure 36). To make use of this, we first used the optical microscope to identify trilayer graphene flakes and then we were able to differentiate clearly ABA and ABC regions, using the Raman microscope (see figures 37 and 38).

This insight is much more valuable, as the current methods of the group do not allow stacking order identification. Moreover, correlated behaviors, as superconductivity, for instance, were recently uncovered in ABC trilayer graphene [32]. According to the chosen research direction, implementing this method could allow the group to fabricate and study ABC based devices.

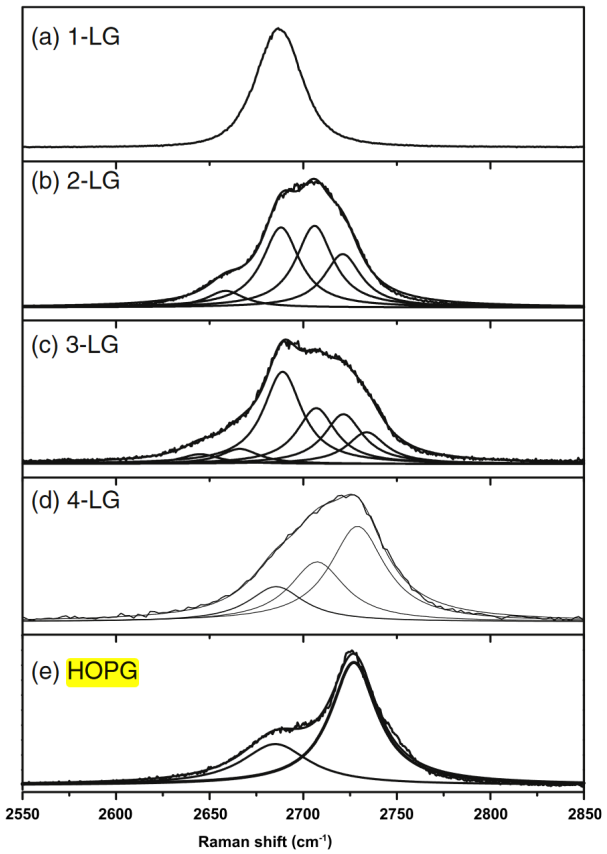

Figure 35: 2D peak dependence as a function of the number of graphene layers. (a) corresponds to single layer graphene, (b), to bilayer, (c), to trilayer, (d), to four layers and (e), to highly oriented pyrolitic graphite. Used excitation wavelength is 514 nm [29].

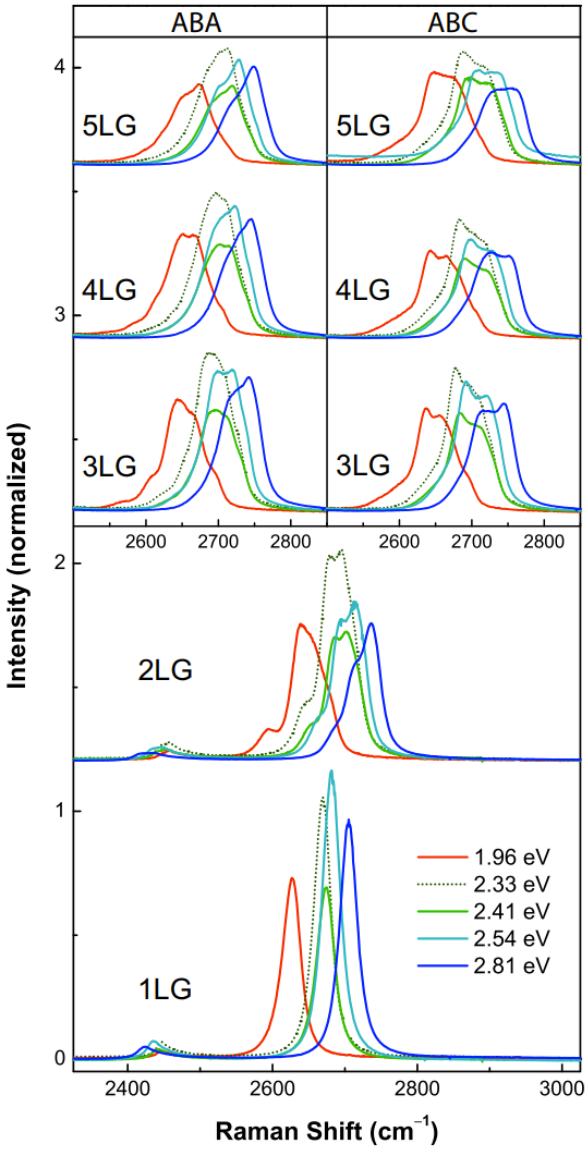

Figure 36: 2D peak dependence as a function of the number of graphene layers and of the stacking order. Our Raman excitation wavelength of 532 nm (2.33 eV) corresponds to the dotted green, showing a significant shape difference between ABA and ABC trilayer [33].

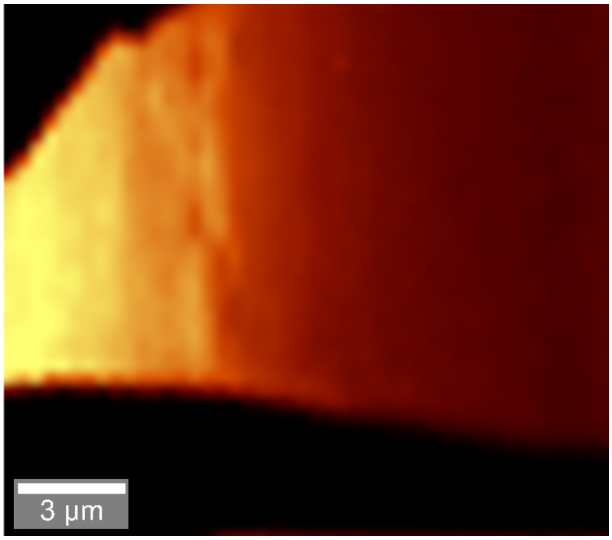

Figure 37: 2D peak intensity map of a trilayer graphene flake. One can see the stacking order phases inside the flake, whose intensity relates to the ABA stacking order-likeness.

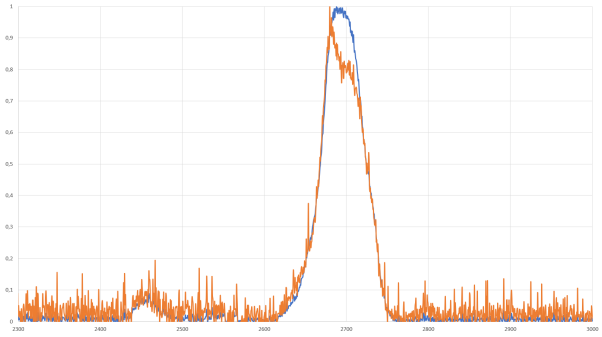

Figure 38: Extracted spectra : the blue one has been extracted from the ABA yellow area of the 2D peak intensity map, while the orange one, from the ABC dark red area. One can recognise the same shapes as in figure 36

3.2 Raman for Laser Cutting

Laser cutting is another useful capability of the Raman microscope. By laser heating very locally a graphene flake, a chemical reaction can be activated between the graphene carbon atoms and atmospheric oxygen to form CO_2 [34]. As a result, this precise burning can accurately be used to achieve cuts thinner than 1 µm.

Laser cutting recently became an accessible method for the group, but it hasn't been much used until now. Even if this method doesn't induce direct mechanic strain on the flakes, it hasn't demonstrated for now much cleaner results than AFM cutting and it loses against AFM manual cutting in terms of practicality.

As the previous method, according to the chosen research direction, implementing this method could be useful and practical to cut graphene flake, in order to isolate ABC regions right after their identification by Raman spectroscopy.

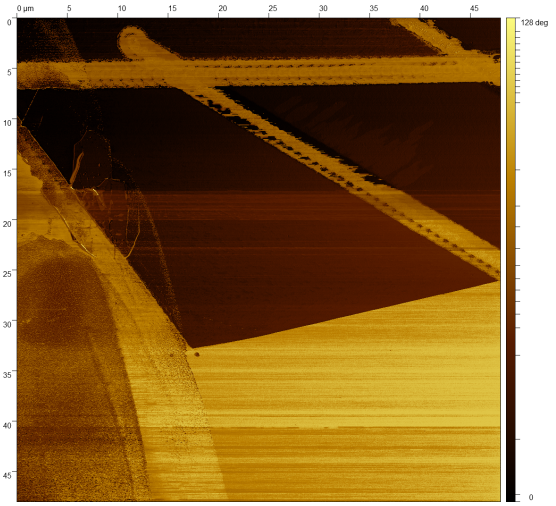

Figure 39: AFM tapping mode measurement of a very intense Raman laser cutting of single layer graphene. The cutting step seems to have greatly put dirtiness onto the graphene.

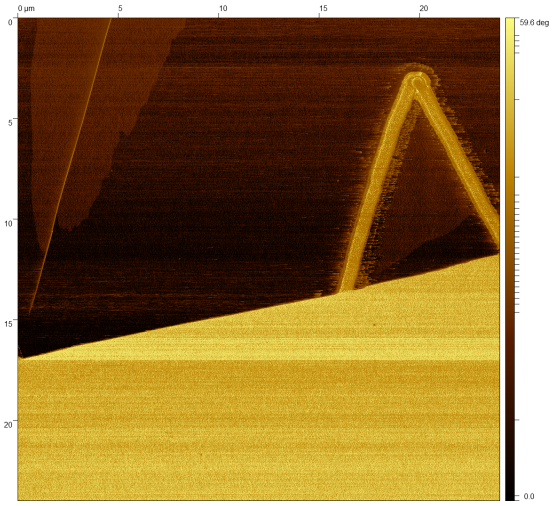

Figure 40: AFM tapping mode measurement of a standard Raman laser cutting of a few layer graphene flake. The cuts are pretty clean and 900 nm wide.

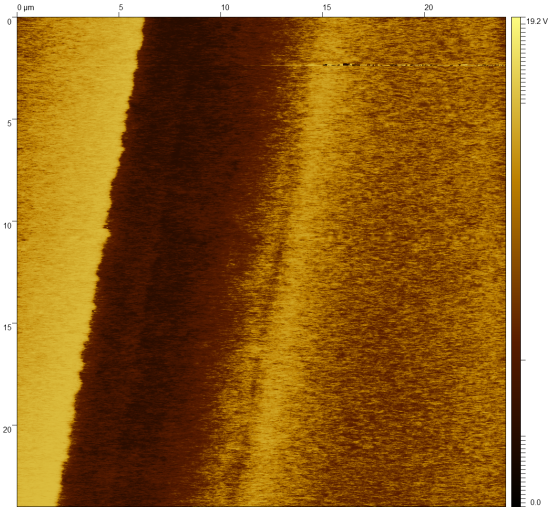

Figure 41: First principle results obtained using peak force KPFM (PF-KPFM). Measured surface potential of a custom metallic sample, made of gold and aluminum deposited on a silicon substrate. The three potential domains correspond to Au, Si and Al surfaces (from left to right).

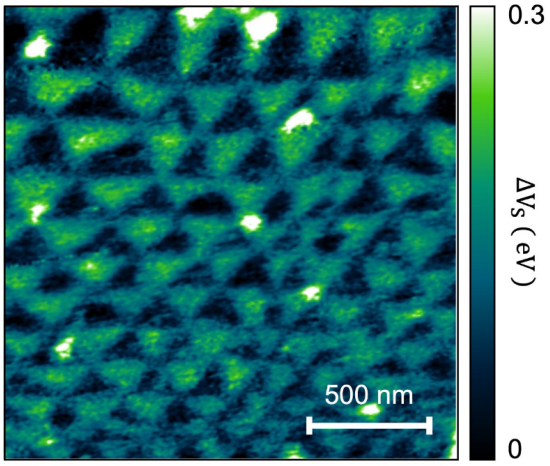

Figure 42: Frequency Modulated KPFM (FM-KPFM) measurement of twisted bilayer hBN, with inhomogeneous twisting angles ranging from 0.03° to 0.3°. The moiré superpotential is clearly visible, characterised by triangular AA and AB regions [35].

3.3 AFM Moiré Imaging

Besides Raman microscopy, I also studied different AFM methods. I got familiar with standard tapping mode and contact mode, before working on the kelvin probe force microscopy (KPFM) modes. The idea is that these modes, dedicated to measuring contact potential difference in the nanometer regime, can be used to image moiré superpotentials [36] (see figure 42).

A surface potential measure was achieved, showing that KPFM measurements could be done with the group tools and motivating subsequent work (see figure 41). For precise graphene measurements, the difficulty also resides in my still in progress fabrication skills. But, this assignment is still underway, with the aim of succeeding moiré imaging of TBG before the end of the internship in september.

3.4 Anodic AFM Cutting

Getting used to the AFM was a very nice preliminary step and it helped me be prepared for the arrival of anodic AFM Cutting tools. The development of this very promising method was the original purpose of my internship and it went very well (see figure 45).

Anodic AFM Cutting is a nanolithography technique, using an AFM conductive tip to induce a chemical very precise etching of graphene layers. The idea is that, when the tip is lifted after making contact with graphene, a nanometer-sized water meniscus is formed, allowing electrically-activated local oxidation [37] (see figure 43). To make this happen, the right conditions are being studied currently, but a typical setup is a relative humidity of 50 % and a lift height of 500 nm.

When the meniscus is formed in between the tip and the graphene flake, a voltage applied to the tip is controlling the rate of the chemical oxidation [38] (see equations 1 and 2). An applied positive voltage results in the graphene being positively charged (anode) and the tip negatively charged (cathode), leading to graphene oxidation above a certain threshold value [**?**].

$$C_{(sol)} + H_20_{(liq)} \longrightarrow CO_{(gas)} + H_{2(gas)} \tag{1}$$

$$C_{(sol)} + 2H_20_{(liq)} \longrightarrow CO_{2(gas)} + 2H_{2(gas)} \tag{2}$$

Shortly after the graphene discovery, this nanolithography process was successfully implemented using a positive DC voltage driven between an AFM tip and an electrically grounded graphene flake [39]. However, this method was far from practical for fabrication : it needed electrical contacts, which had to be chemically removed before stacking. The needed steps (PMMA coating, EBL, metallic evaporation and chemical cleaning) were occurring directly on an uncovered graphene flake and this process was very detrimental to its cleanliness.

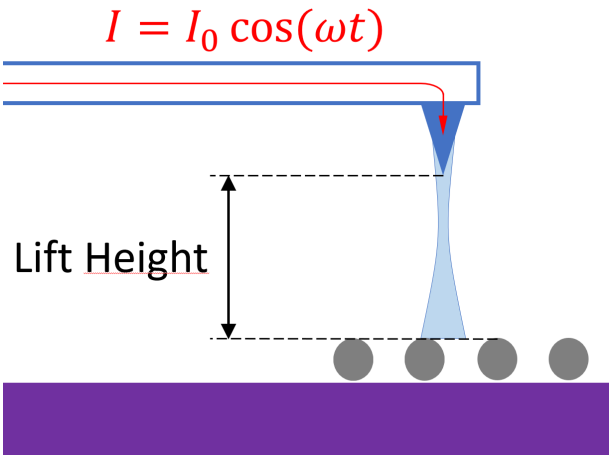

Figure 43: Sketch of the anodic AFM cutting method. The water meniscus (in pale blue) appears when the tip (in dark blue) is lifted from the graphene (in grey), allowing oxidation reaction to take place.

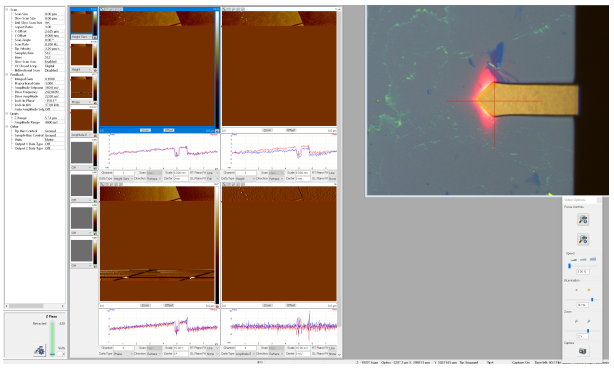

Figure 44: Picture of AFM tapping mode interface. After the anodic cutting, using a particular tip, it is changed to a standard tapping mode tip to measure the cuts. Swapping the tip like that helps to prevent anodic cutting tips from wearing off too fast, which would widen the next cuts.

Nonetheless, a new electrode-free anodic oxidation process was presented in 2018, using the exact same principle, but associated to a high-frequency AC voltage [40]. The idea is that, on one hand, when the voltage on the tip is positive above the oxidation threshold, the graphene is etched, generating gaseous products only. On the other hand, when the voltage is negative, any unwanted oxidation-reduction reaction is prevented by a special coating of the tip. For instance, one can use a gold, iridium or platinum coated AFM tip to prevent it from oxidising.

The biggest benefit comes from the electrode-free process, thanks to the application of this high-frequency AC voltage. The thick Si layer of the silicon substrate can be considered grounded and separated from the graphene flake by a thin SiO_2 dielectric layer. From this point of view, the AC voltage is driving an alternating current from the tip to the flake and from the flake through the dielectric in the form of a displacement current. Then, the use of electrodes grounding the flake isn't necessary, which is simplifying the process and keeping the flake very clean.

Furthermore, anodic cutting recently gave very promising results, with a research group achieving very clean sub-100 nm patterned features in graphite gates [41][42]. Its first versatile capability is the possibility to cut any FLG : they reported, for instance, very precise cuts in a 3 nm thick graphite flake (about 9 graphene layers). Second is the wideness of the cuts, as thin as 70 nm, coupled to the cleanliness of the picked up flake, allowing numerous interesting designs, as a quantum point contact geometry, for instance.

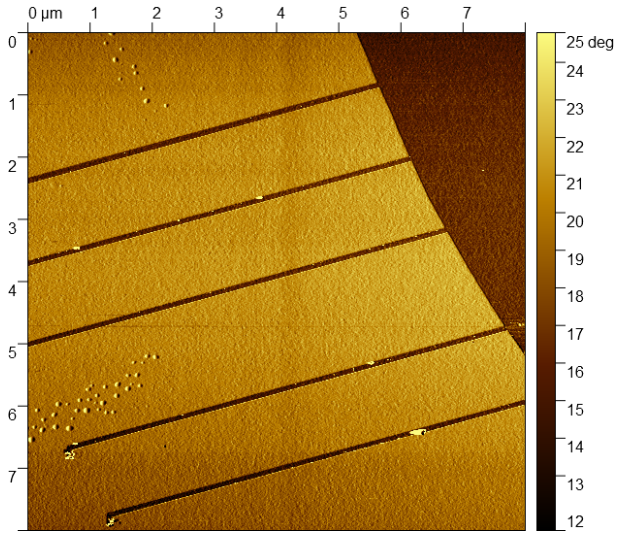

Figure 45: AFM tapping mode phase map of a bilayer flake after anodic oxidation cutting. The cuts are almost perfectly clean (at least, from the AFM standpoint), with still some solid dirt particles appearing inside the cuts. According to recent results, these dirt particles stick to the substrate and a perfectly clean flake can be obtained when picked up [41][42].

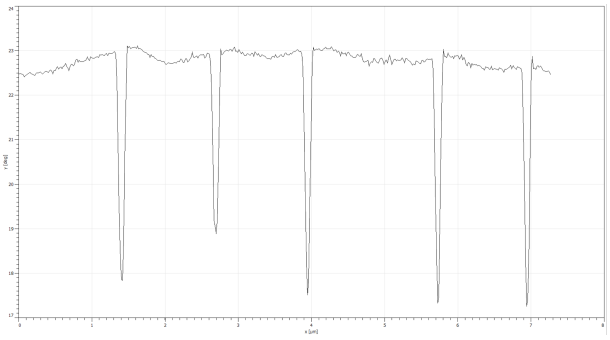

Figure 46: AFM tapping mode phase measurement of the bilayer cuts. Here, the well defined cuts are 120 nm wide on average, with two 100 nm wide cuts.

• Towards New Projects in the Group

During the past month, anodic AFM cutting was successfully implemented with the group tools. It was used to achieve first principle implementation by cutting single layer and bilayer graphene flakes. I'm still working on understanding and fine-tuning the cutting parameters : until now, I managed to set the group record at 120 nm wide cuts (see figures 44, 45 and 46). Until the end of my internship, I will gladly continue to work on this and, with Christian Obermayer (technical assistant) and Jaime Díez-Mérida (PhD student), we'll try to truly implement this method in order to get an actual device.

These multiple new methods were a perfect fit for my temporary position in the group, it was very nice for me to discover the field, the fabrication process and what each member of the group was doing. According to the next chosen directions of research, these methods could be very useful for the group and they will still remain a valuable asset in the long run.

In the short term, one actual implementation of the anodic AFM cutting technique could be to design a Josephson junction (JJ) gate geometry in a MATBG superconducting device. I'll try to use my time left in the group to continue learning about this subject of research and to see if it could be an interesting development of the current work of Jaime Díez-Mérida and Andres Díez-Carlón (PhD Student) [26].

RÉFÉRENCES

[1] K. S. Novoselov, A. K. Geim, S. V. Morozov, D. Jiang, Y. Zhang, S. V. Dubonos, I. V. Grigorieva, and A. A. Firsov, "Electric field effect in atomically thin carbon films," vol. 306, no. 5696, pp. 666–669, publisher : American Association for the Advancement of Science. [Online]. Available : https://www.science.org/doi/10.1126/science.1102896

[2] K. S. Novoselov, A. K. Geim, S. V. Morozov, D. Jiang, M. I. Katsnelson, I. V. Grigorieva, S. V. Dubonos, and A. A. Firsov, "Two-dimensional gas of massless dirac fermions in graphene," vol. 438, no. 7065, pp. 197–200, number : 7065 Publisher : Nature Publishing Group. [Online]. Available : https://www.nature.com/articles/nature04233

[3] Y. Cao and P. Jarillo-Herrero, "Unconventional superconductivity in magic-angle graphene superlattices." [Online]. Available : https://www.nature.com/articles/nature26160

[4] L. Linnala, "Electron assisted growth of graphene atop ir(111) supported hexagonal boron nitride."

[5] A. K. Geim and K. S. Novoselov, "The rise of graphene," vol. 6, no. 3, pp. 183–191, number : 3 Publisher : Nature Publishing Group. [Online]. Available : https://www.nature.com/articles/nmat1849

[6] F. Kusmartsev, W. Wu, M. Pierpoint, and W. Yung, "Application of graphene within optoelectronic devices and transistors."

[7] A. Maffucci and G. Miano, "Electrical properties of graphene for interconnect applications," vol. 4, pp. 305–317.

[8] J. González, "Kohn-luttinger superconductivity in graphene," vol. 78, no. 20, p. 205431, publisher : American Physical Society. [Online]. Available : https://link.aps.org/doi/10.1103/PhysRevB.78.205431

[9] W. Kohn and J. M. Luttinger, "New mechanism for superconductivity," vol. 15, no. 12, pp. 524–526, publisher : American Physical Society. [Online]. Available : https://link.aps.org/doi/10.1103/PhysRevLett.15.524

[10] D. K. Efetov, "Towards inducing superconductivity into graphene." [Online]. Available : https://doi.org/10.7916/D8VX0F3T

[11] K. Björnson. The band structure of graphene. Section : Uncategorized. [Online]. Available : https://second-tech.com/wordpress/index.php/2019/07/05/the-graphene-band-structure/

[12] G. Li, A. Luican, J. M. B. Lopes dos Santos, A. H. Castro Neto, A. Reina, J. Kong, and E. Y. Andrei, "Observation of van hove singularities in twisted graphene layers," vol. 6, no. 2, pp. 109–113, number : 2 Publisher : Nature Publishing Group. [Online]. Available : https://www.nature.com/articles/nphys1463

[13] J. M. B. Lopes dos Santos, N. M. R. Peres, and A. H. Castro Neto, "Graphene bilayer with a twist : Electronic structure," vol. 99, no. 25, p. 256802, publisher : American Physical Society. [Online]. Available : https://link.aps.org/doi/10.1103/PhysRevLett.99.256802

[14] R. Bistritzer and A. H. MacDonald, "Moiré bands in twisted double-layer graphene," vol. 108, no. 30, pp. 12 233–12 237, publisher : Proceedings of the National Academy of Sciences. [Online]. Available : https://www.pnas.org/doi/10.1073/pnas.1108174108

[15] E. Suárez Morell, J. D. Correa, P. Vargas, M. Pacheco, and Z. Barticevic, "Flat bands in slightly twisted bilayer graphene : Tight-binding calculations," vol. 82, no. 12, p. 121407, publisher : American Physical Society. [Online]. Available : https://link.aps.org/doi/10.1103/PhysRevB.82.121407

[16] Y. Cao, V. Fatemi, A. Demir, S. Fang, S. L. Tomarken, J. Y. Luo, J. D. Sanchez-Yamagishi, K. Watanabe, T. Taniguchi, E. Kaxiras, R. C. Ashoori, and P. Jarillo-Herrero, "Correlated insulator behaviour at half-filling in magic-angle graphene superlattices," vol. 556, no. 7699, pp. 80–84, number : 7699 Publisher : Nature Publishing Group. [Online]. Available : https://www.nature.com/articles/nature26154

[17] X. Lu, P. Stepanov, W. Yang, M. Xie, M. A. Aamir, I. Das, C. Urgell, K. Watanabe, T. Taniguchi, G. Zhang, A. Bachtold, A. H. MacDonald, and D. K. Efetov, "Superconductors, orbital magnets and correlated states in magic-angle bilayer graphene," vol. 574, no. 7780, pp. 653–657, number : 7780 Publisher : Nature Publishing Group. [Online]. Available : https://www.nature.com/articles/s41586-019-1695-0

[18] P. Stepanov, M. Xie, T. Taniguchi, K. Watanabe, X. Lu, A. MacDonald, B. A. Bernevig, and D. Efetov, "Competing zero-field chern insulators in superconducting twisted bilayer graphene," vol. 127, no. 19, p. 197701, publisher : American Physical Society. [Online]. Available : https://link.aps.org/doi/10.1103/PhysRevLett.127.197701

[19] M. Serlin, C. L. Tschirhart, H. Polshyn, Y. Zhang, J. Zhu, K. Watanabe, T. Taniguchi, L. Balents, and A. F. Young. Intrinsic quantized anomalous hall effect in a moiré heterostructure. [Online]. Available : https://www.science.org/doi/10.1126/science.aay5533

[20] Y. Huang, E. Sutter, N. N. Shi, J. Zheng, T. Yang, D. Englund, H.-J. Gao, and P. Sutter, "Reliable exfoliation of large-area high-quality flakes of graphene and other two-dimensional materials," vol. 9, no. 11, pp. 10 612–10 620, publisher : American Chemical Society. [Online]. Available : https://doi.org/10.1021/acsnano.5b04258

[21] P. Blake, E. W. Hill, A. H. Castro Neto, K. S. Novoselov, D. Jiang, R. Yang, T. J. Booth, and A. K. Geim, "Making graphene visible," vol. 91, no. 6, p. 063124. [Online]. Available : https://pubs.aip.org/apl/article/91/6/063124/1023191/Making-graphene-visible

[22] J. Hwang, C. Zhang, Y.-S. Kim, R. Wallace, and K. Cho, "Giant renormalization of dopant impurity levels in 2d semiconductor MoS2," vol. 10.

[23] C. R. Dean, A. F. Young, I. Meric, C. Lee, L. Wang, S. Sorgenfrei, K. Watanabe, T. Taniguchi, P. Kim, K. L. Shepard, and J. Hone, "Boron nitride substrates for high-quality graphene electronics," vol. 5, no. 10, pp. 722–726, number : 10 Publisher : Nature Publishing Group. [Online]. Available : https://www.nature.com/articles/nnano.2010.172

[24] A. S. Mayorov, R. V. Gorbachev, S. V. Morozov, L. Britnell, R. Jalil, L. A. Ponomarenko, P. Blake, K. S. Novoselov, K. Watanabe, T. Taniguchi, and A. K. Geim, "Micrometer-scale ballistic transport in encapsulated graphene at room temperature,"

vol. 11, no. 6, pp. 2396–2399, publisher : American Chemical Society. [Online]. Available : https://doi.org/10.1021/nl200758b

[25] M. Kim, S. G. Xu, A. I. Berdyugin, A. Principi, S. Slizovskiy, N. Xin, P. Kumaravadivel, W. Kuang, M. Hamer, R. K. Kumar, R. V. Gorbachev, K. Watanabe, T. Taniguchi, I. V. Grigorieva, V. I. Fal'ko, M. Polini, and A. K. Geim, "Control of electron-electron interaction in graphene by proximity screening," vol. 11, no. 1, p. 2339. [Online]. Available : http://arxiv.org/abs/1911.10128

[26] J. Díez-Mérida, A. Díez-Carlón, S. Y. Yang, Y.-M. Xie, X.-J. Gao, J. Senior, K. Watanabe, T. Taniguchi, X. Lu, A. P. Higginbotham, K. T. Law, and D. K. Efetov, "Symmetry-broken josephson junctions and superconducting diodes in magic-angle twisted bilayer graphene," vol. 14, no. 1, p. 2396, number : 1 Publisher : Nature Publishing Group. [Online]. Available : https://www.nature.com/articles/s41467-023-38005-7

[27] L. Wang, I. Meric, P. Y. Huang, Q. Gao, Y. Gao, H. Tran, T. Taniguchi, K. Watanabe, L. M. Campos, D. A. Muller, J. Guo, P. Kim, J. Hone, K. L. Shepard, and C. R. Dean, "One-dimensional electrical contact to a two-dimensional material," vol. 342, no. 6158, pp. 614–617.

[28] L. Aoyagi, "Fermi liquid behavior in twisted bilayer graphene."

[29] L. M. Malard, M. A. Pimenta, G. Dresselhaus, and M. S. Dresselhaus, "Raman spectroscopy in graphene," vol. 473, no. 5, pp. 51–87. [Online]. Available : https://www.sciencedirect.com/science/article/pii/S0370157309000520

[30] N. Poklonski, E. Kislyakov, S. Vyrko, O. Bubel, and S. Ratkevich, "Electronic band structure and magnetic states of zigzag graphene nanoribbons : Quantum chemical calculations," vol. 6, pp. 061 712–1(9).

[31] L. G. Cançado, M. A. Pimenta, B. R. A. Neves, M. S. S. Dantas, and A. Jorio, "Influence of the atomic structure on the raman spectra of graphite edges," vol. 93, no. 24, p. 247401, publisher : American Physical Society. [Online]. Available : https://link.aps.org/doi/10.1103/PhysRevLett.93.247401

[32] H. Zhou, T. Xie, T. Taniguchi, K. Watanabe, and A. F. Young, "Superconductivity in rhombohedral trilayer graphene," vol. 598, no. 7881, pp. 434–438, number : 7881 Publisher : Nature Publishing Group. [Online]. Available : https://www.nature.com/articles/s41586-021-03926-0

[33] T. A. Nguyen, J.-U. Lee, D. Yoon, and H. Cheong, "Excitation energy dependent raman signatures of ABA- and ABC-stacked few-layer graphene," vol. 4, no. 1, p. 4630, number : 1 Publisher : Nature Publishing Group. [Online]. Available : https://www.nature.com/articles/srep04630

[34] R. Stöhr, R. Kolesov, and K. Xia, "All-optical high-resolution nanopatterning and 3d suspending of graphene," vol. 5, pp. 5141–50.

[35] D. S. Kim, R. Dominguez, R. Mayorga-Luna, D. Ye, J. Embley, T. Tan, Y. Ni, Z. Liu, M. Ford, F. Gao, S. Arash, K. Watanabe, T. Taniguchi, S. Kim, C. Shih, K. Lai, W. Yao, L. Yang, X. Li, and Y. Miyahara, Electrostatic moir\'e potential from twisted-hBN layers.

[36] BRUKER. PeakForce KPFM. [Online]. Available : https://www.bruker.com/en/products-and-solutions/microscopes/materials-afm/afm-modes/pf-kpfm.html

[37] B. Weeks, M. Vaughn, and J. DeYoreo, "Direct imaging of meniscus formation in atomic force microscopy using environmental scanning electron microscopy," vol. 21, no. 18, publisher : Langmuir. [Online]. Available : https://pubmed.ncbi.nlm.nih.gov/16114907/

[38] W. Han, P. T. Mathew, S. Kolagatla, B. Rodriguez, and F. Fang, "Toward single-atomic-layer lithography on highly oriented pyrolytic graphite surfaces using AFM-based electrochemical etching," vol. 5.

[39] L. Weng, L. Zhang, Y. P. Chen, and L. P. Rokhinson, "Atomic force microscope local oxidation nanolithography of graphene," vol. 93, no. 9, p. 093107. [Online]. Available : https://doi.org/10.1063/1.2976429

[40] H. Li, Z. Ying, B. Lyu, A. Deng, L. Wang, T. Taniguchi, K. Watanabe, and Z. Shi, "Electrode-free anodic oxidation nanolithography of low-dimensional materials," vol. 18, no. 12, pp. 8011–8015.

[41] L. Cohen, N. Samuelson, T. Wang, T. Taniguchi, K. Watanabe, M. Zaletel, and A. Young, Universal chiral Luttinger liquid behavior in a graphene fractional quantum Hall point contact.

[42] L. A. Cohen, N. L. Samuelson, T. Wang, K. Klocke, C. C. Reeves, T. Taniguchi, K. Watanabe, S. Vijay, M. P. Zaletel, and A. F. Young, "Tunable fractional quantum hall point contacts in graphene via local anodic oxidation of graphite gates." [Online]. Available : http://arxiv.org/abs/2204.10296